The Influence of Time-Dependent Melting on the Dynamics and Precipitation Production in Maritime and Continental Storm Clouds

VAUGHAN T. J. PHILLIPS

Atmospheric and Oceanic Sciences Program, Princeton University, Princeton, New Jersey

ANDREI POKROVSKY AND ALEXANDER KHAIN

Institute of Earth Sciences, Hebrew University of Jerusalem, Jerusalem, Israel

(Manuscript received 13 June 2005, in final form 3 February 2006)

ABSTRACT

Simulations of one maritime and four continental observed cases of deep convection are performed with the Hebrew University Cloud Model that has spectral bin microphysics. The maritime case is from observations made on 18 September 1974 during the Global Atmospheric Research Program's Atlantic Tropical Experiment (GATE). The continental storm cases are those of summertime Texas clouds observed on 13 August 1999, and green-ocean, smoky, and pyro-clouds observed during the Large-Scale Biosphere–Atmosphere Experiment in Amazonia–Smoke, Aerosols, Clouds, Rainfall, and Climate (LBA–SMOCC) campaign on 1–4 October 2002. Simulations have been performed for these cases with a detailed melting scheme. This scheme allows calculation of liquid water fraction within each mass bin for the melting of graupel, hail, snowflakes, and crystals, as well as alteration of the sedimentation velocity of ice particles in the course of their melting. The results obtained with the detailed melting scheme are compared with corresponding results from simulations involving instantaneous melting at the freezing (0°C) level.

The detailed melting scheme allows penetration of ice from the freezing level down into the boundary layer by distances ranging from a few hundred meters for the numerous, smaller particles to ~1.5 km for the largest particles, which are much scarcer. In these simulations, most of the mass of ice falling out melts over this short distance of a few hundred meters. The deepening and intensification of the layer of latent cooling enhances the convective destabilization of the troposphere. This effect is especially pronounced under continental conditions, causing significant changes in the accumulated rain amount.

1. Introduction

Destabilization of the atmosphere may be caused by latent cooling from melting (Findeisen 1940; Moore and Stewart 1985; Rauber et al. 2000). When ice melts, there is absorption of latent heat which cools the ambient air. The existence of isothermal layers at 0°C due to melting ice, and consequent convective instability, was first recognized by Findeisen (see also Wexler et al. 1954; Willis and Heymsfield 1989). Marwitz (1983) and Szeto et al. (1988) have reported that isothermal layers caused by melting can be up to 1 km deep. The generation of convection by melting-induced cooling can produce extra clouds (fractocumulus) as the reduced lapse rate within an isothermal layer causes a steepening of the lapse rate beneath it (e.g., Findeisen 1940; Stewart et al. 1984; Knight et al. 2004).

The process of melting is not instantaneous: latent heat of melting must be provided to the ice core of a melting particle. This heat can only be supplied at a finite rate. At a steady state, it is equal to the rate of heat transfer through the layer of meltwater to the ice core. This, in turn, is balanced by the net rate of supply of heat though the air to its liquid surface by forced convection and evaporation (or condensation; Pruppacher and Klett 1997, hereafter PK97). Smaller ice particles melt away more quickly and at levels nearer to the freezing level, compared to larger ones (Willis and Heymsfield 1989). Their higher surface area-to-mass ratio boosts the supply of latent heat of melting to their ice core, as the rate of heat transfer is proportional to the surface area of the particle (PK97). Consequently,

Corresponding author address: Vaughan Phillips, Geophysical Fluid Dynamics Laboratory, NOAA/OAR Dept. of Commerce, Princeton Forrestal Campus, P.O. Box 308, Princeton, NJ 08540. E-mail: vaughan.phillips@noaa.gov

DOI: 10.1175/JAS3832.1

only hail, graupel, or snow can typically reach the ground when the freezing level is a few kilometers above it.

The ice phase is important for the generation of precipitation in many types of convective system, especially in midlatitudes (Szyrmer and Zawadzki 1999). Generally, high CCN concentrations promote formation of ice-phase precipitation by cold-cloud processes (i.e., by vapor growth, riming, and aggregation) in deep convective and orographic clouds, causing copious melting during fallout (Reisin et al. 1996; Chen and Lamb 1999; Khain and Pokrovsky 2004). The fraction of total surface precipitation from melting was 50% for maritime aerosols in simulations of deep convective cloud by Khain and Pokrovsky (2004), and increased with the environmental CCN concentration. The ice phase may also be generated by the warm rain process and raindrop freezing in deep convective clouds (Phillips et al. 2001). For a subtropical squall line simulated by Tao et al. (1991), inclusion of the ice phase was needed for it to persist longer than 4 h. Extreme values of surface precipitation rate increased by about 50% when the ice phase was excluded in a thunderstorm simulated by Ziegler (1988).

The mesoscale dynamics of the atmosphere have been shown to be modified by the melting of ice precipitation in field experiments (Atlas et al. 1969; Stewart and Macpherson 1989; Stewart et al. 1996; Knight et al. 2004) and numerical simulations (e.g., Chen and Cotton 1988; Szeto et al. 1988; Szyrmer and Zawadzki 1999). Liu et al. (1997) identify three possible mechanisms for how the ice phase influences a storm's dynamics: 1) melting-induced latent cooling strengthens downdrafts, while freezing strengthens updrafts; 2) the vertical lapse rate is altered by latent heating/cooling, which can cause atmospheric instability (e.g., Findeisen 1940; Wexler et al. 1954); and 3) the much lower terminal velocity of ice particles relative to raindrops of the same mass causes water substance to be transported farther horizontally during fallout, forming widespread anvils downshear from the deep convection.

Concerning mechanism 1, the dynamical structure of any system of organized convection is a response of a shear flow to heating and cooling, to which melting contributes substantially (e.g., Tao et al. 1991). Descent driven by melting-induced cooling causes formation of the subcloud cold pool beneath squall-type systems (Liu et al. 1997) and rainbands (Barth and Parsons 1996). The cold pool determines circulations within a storm and promotes formation of new cells. Melting-induced downdrafts intensify the low-level horizontal convergence in warm frontal precipitation systems, accelerating surface frontogenesis and invigorating updrafts (Szeto and Stewart 1997). For mechanism 2, Knight et al. (2004) have observed initiation by cooling in the melting layer of weakly convective elements. Regarding mechanism 3, the coverage of stratiform anvil cloud is increased by the presence of ice particles (Barth and Parsons 1996; Tao et al. 1991; Liu et al. 1997) owing to their low fall speeds.

There are some curious physical phenomena that occur during melting. First, the onset of melting is delayed if particles fall through the freezing (0°C) level in a subsaturated environment. Evaporation temporarily absorbs all the heat supplied by forced convection from the environment, preventing melting. For instance, at a relative humidity of 50%, melting only begins at 4°C (PK97). Second, the terminal velocity of graupel and hail is increased by the initial wetting of their surface, but can be subsequently reduced if a "meltwater torus" develops around the equator of the particle.

Such subtle aspects of melting are represented in a detailed melting procedure that has been implemented in the Hebrew University Cloud Model (HUCM), which is a spectral microphysics model. This scheme extends the scheme applied by Phillips (2001, p. 76) and Phillips et al. (2001, 2002, 2003, 2005). The procedure takes into account processes of diffusion of heat into the melting particles and the modification of the terminal velocity of particles during melting.

Accurate representation of melting is important for simulating the radar bright band of stratiform melting layers (e.g., Bauer et al. 2000). The radar reflectivity is high in the bright band (e.g., Wexler et al. 1954) because (Battan 1973, 190–195; Klaassen 1988): 1) melting particles are covered by a film of water, so they reflect as effectively as liquid drops, and 2) their volume and surface area are higher than drops of the same mass because of their lower bulk density and nonspherical shape (e.g., Fabry and Szyrmer 1999), increasing their backscatter cross section and causing a lower terminal velocity and higher number density. Precipitation growth/breakup may also contribute slightly (Fabry and Zawadzki 1995).

In the present paper, impacts on the precipitation production and dynamics of cloud caused by the time-dependent process of melting are examined with a powerful new tool, the detailed melting scheme. Such a scheme permits a highly accurate simulation of the rate of melting of ice and of the spatial distribution of melting-induced cooling. Variations in the terminal velocity of particles during melting, and associated changes in their shape, size, and surface smoothness, are represented in this scheme; such details were typically neglected in previous modeling studies. A tropical maritime case, and some continental cases when clouds

develop in extremely polluted air, are simulated. The model is described in the next section. In sections 3–6, results from sensitivity tests with respect to inclusion of the detailed melting scheme are presented and discussed.

2. The model

The HUCM is a two-dimensional nonhydrostatic model with spectral bin microphysics. The equations for velocity components, and the continuity equation, are expressed in terms of the vorticity and streamfunction. Thermodynamic equations include the equations for the potential temperature and vapor mixing ratio.

Size distributions for several microphysical species are predicted, in the HUCM, with 33 mass doubling categories for each microphysical species. These species are water drops, ice crystals (three types), aggregates, graupel, frozen drops/hail, and aerosols playing the role of cloud condensational nuclei (CCN). Further details about the HUCM are given by Khain and Sednev (1996) and Khain et al. (2000, 2004).

The new detailed melting scheme in the HUCM is based on models by 1) Mitra et al. (1990) for crystals/snow and 2) Rasmussen et al. (1984a) and Rasmussen and Heymsfield (1987, hereafter RH87) for graupel/hail. The overall principle is that the heat budget of the particle determines its melting rate. The heat budget includes diffusion of heat and (vapor) mass to and from the particle.

For all ice, melting is only allowed to start when the surface temperature attains the value of 273.15 K. Melting may be further delayed due to evaporative cooling (see PK97). While the surface of the ice is dry, before the onset of melting, sublimation is assumed to occur. This sublimation causes a pronounced latent cooling. After melting has commenced, evaporation of meltwater occurs instead of sublimation, also causing a latent cooling.

Melted liquid water in each mass bin of ice particles is advected with the particles. If an ice particle with a nonzero liquid water fraction (LWF) penetrates into the region of subzero temperatures, the LWF is set to zero (i.e., the water freezes). Adjustment of the ambient temperature and humidity is performed by the melting scheme as a result of the phase changes of melting, sublimation, and evaporation.

Furthermore, adjustment of the terminal fall velocity of ice particles by the presence of meltwater is represented. Whereas for snow and crystals there is a monotonic increase of the terminal velocity with LWF during melting, the situation is more complex for hail and graupel. At the onset of melting, their surface becomes wet. Consequently, hail or graupel with Reynolds numbers <4000 displays a sudden increase in terminal velocity as the drag coefficient suddenly becomes that of a smooth sphere. But after the ice particle is fully soaked with meltwater, the shape of the particle is affected by meltwater being aerodynamically molded. Any buildup of a meltwater torus can tend to reduce the fall speed.

a. Melting of crystals and snow

Snow particles are assumed to be spheroidal with an axial ratio that changes during melting from 0.3, the dry value, toward unity. The ice is assumed to have an incollapsible "skeleton" structure, with meltwater accumulating in the interior of the ice structure.

Before melting starts, there may be sublimation of (or vapor deposition onto) the dry ice particle, which cools (or warms) it relative to the ambient air. An iterative technique produces a value for the surface temperature of the ice (Mitra et al. 1990):

$$T_s = \min\{T - [L_s D_v/(k_a R_v)][e_{\mathrm{sat},i}(T_s)/T_s - e/T],\ T_0\}. \tag{1}$$

Here T is the ambient air temperature, e is the ambient vapor pressure, L_s is the latent heat of sublimation, D_v is the diffusivity of water vapor, k_a is that of heat, R_v is the gas constant for vapor, and $e_{\mathrm{sat},i}$ is the saturated vapor pressure over ice, while $T = 273.15$ K (0°C). The iterative equation (1) is obtained by equating rates for the absorption of heat by sublimation and for the supply of heat by convection through surrounding air.

Melting of an ice particle begins only when the temperature at the surface of its skeleton, T_s, reaches 0°C. It is assumed that this temperature is uniform across the entire surface of the skeleton. Once melting has begun, the change in mass of ice in time step dt is

$$dm_i = -dt(4\pi C_i f_v/L_m)[k_a(T - T_0) + (D_v L_e/R_v) \times (e/T - e_{\mathrm{sat},w}(T)/T)]. \tag{2}$$

Here, L_m and L_e are the latent heats of melting and evaporation, while $e_{\mathrm{sat},w}$ is the saturated vapor pressure over water and f_v is the ventilation coefficient for vapor. Of course, dm_i is negative when there is actual melting. However, it may also be positive if evaporative cooling delays the onset of melting. Any liquid on the surface is then frozen. During melting, it is assumed that $T_s = T_0$. This is because it is not possible for T_s to exceed T_0, as the skeleton is ice. Also, if $T_s < T_0$, then the surface of the ice skeleton must cease to melt, so the entire particle must cease to melt. [Generally, melting of a bulk mass of solid ice of any shape must be located at its surface; otherwise, heat supplied by the surrounding air would have to flow by conduction through the interior

of the ice from the (colder) temperature $T_s < T_0$ of the nonmelting surface to the (warmer) temperature T_0 of any melting region in the interior as melting absorbs latent heat, which would be impossible.] Also, the assumption that the meltwater has a temperature of T_0 during melting, which is empirically based, is inherent in (2) (PK97, p. 693).

For snow, the ventilation coefficients with respect to transfer of vapor and heat are assumed to be identical. The ventilation coefficient for vapor is

$$f_v = 1 + 0.14\chi^2, \quad \chi < 1$$
$$0.86 + 0.28\chi, \quad \chi > 1, \tag{3}$$

where $\chi = N_{\mathrm{Sc}}^{1/3} N_{\mathrm{Re}}^{1/2}$. The Reynolds and Schmidt numbers are

$$N_{\mathrm{Re}} = L^* v_i \rho/\eta_a; \quad N_{\mathrm{Sc}} = \eta_a/(\rho D_v), \tag{4}$$

where η_a is the dynamic viscosity, L^* is the ratio of the surface area of the flake to its perimeter, and ρ is the density of the air. The fall speed, v_i, is empirically determined:

$$v_i = v_{i,0} + (v_R - v_{i,0})X(\mathrm{LWF}), \tag{5}$$

where X is an empirical function of the liquid water fraction, $\mathrm{LWF} = m_w/(m_i + m_w)$ (Mitra et al. 1990), and $v_{i,0}$ is the terminal velocity just before melting begins. The terminal velocity changes during melting because the drag force is reduced by changes in the overall shape and size of the melting particle while its surface is wet, and therefore smooth. Also, $v_{i,0}$ and v_R are the hypothetical fall speed of the dry (unmelted) and fully melted snow particle, respectively. The fall speed of fully melted particles is equal to that of a raindrop of the same mass as the melting particle.

The melting snow particle is assumed to be an oblate spheroid of variable axial ratio, AR_i. The idealized capacitance of the dry particle, if assumed to be spheroidal, is

$$C_{i,0} = a_i \varepsilon_i / \sin^{-1}(\varepsilon_i), \tag{6}$$

where $\varepsilon_i = (1 - AR_i^2)^{1/2}$ with the equatorial radius of the ice particle being $a_i = [3(m_i/\rho_i)/(4\pi AR_i)]^{1/3}$. The actual capacitance during melting, proposed by Mitra et al. (1990), is

$$C_i = C_{i,0}(0.8 + 0.2\mathrm{LWF}). \tag{7}$$

Note that the actual dry capacitance is 80% of the idealized value, $C_{i,0}$, due to deviations of the real ice particles from a perfectly spheroidal shape. The axial ratio is also interpolated with respect to the liquid fraction:

$$\mathrm{AR}_i = \mathrm{AR}_{i,0} + (1 - \mathrm{AR}_{i,0})\mathrm{LWF}. \tag{8}$$

For snow, $\mathrm{AR}_{i,0} = 0.3$, where $\mathrm{AR}_{i,0}$ is the initial axial ratio of the dry particle. The bulk density of the ice component, ρ_i, (not including meltwater) does not change during melting and is equal to the bulk density of the dry particle.

If LWF > 0, then meltwater evaporates (condenses):

$$dm_w = -[dm_i L_m + dt(4\pi C_i f_v)k_a(T - T_0)]/L_e. \tag{9}$$

This expression is obtained by substituting $dm_w/dt = (4\pi C_i f_v)\ (D_v/R_v)\ (e/T - e_{\mathrm{sat},w}(T_0)/T_0)$ [from Eqs. (13)–(10), (13)–(49) in PK97] into Eq. (2). If LWF = 0, before melting has begun, there is sublimation (vapor deposition):

$$dm_i = dt(4\pi C_i f_v)(e/e_{\mathrm{sat},i}(T_s) - 1)/\zeta. \tag{10}$$

Here, $\zeta = [L_S/(R_v T) - 1]L_S/(k_a T) + R_v T/(e_{\mathrm{sat},i}(T_s)D_v)$ [see Eqs. (13)–(76) and (13)–(85) of PK97].

Crystals are treated in the same way as for snow, with three main exceptions. First, their dry axial ratio, $\mathrm{AR}_{i,0} = h/d$ or L/d, is prescribed in the melting scheme from the following empirical formulas:

- $m_{i,0}(g) = 0.0376\ d(\mathrm{cm})^{3.31}$ and $h(\mathrm{cm}) = 0.0141\ d(\mathrm{cm})^{0.474}$ for plates (see "Pla" in Tables 2.2a and 2.4a of PK97),
- $m_{i,0}(\mathrm{g}) = 0.00376\ d(\mathrm{cm})^{2.79}$ and $h(\mathrm{cm}) = 0.00996\ d(\mathrm{cm})^{0.415}$ for dendrites (see "Plc" in Tables 2.2a and 2.4a of PK97),
- $m_{i,0} = \rho_i(\pi/4)d^2L$ and $d(\mathrm{mm}) = 0.5\ L(\mathrm{mm})$ (size < 0.3 mm) or $d(\mathrm{mm}) = 0.1973L(\mathrm{mm})^{0.414}$ (size > 0.3 mm), for columns (see Table 2.5 of PK97).

For columns, $\mathrm{AR}_{i,0}$ is confined to the range from 2 to 5. Second, for columns, the dry capacitance is determined as for a prolate spheroid:

$$C_{i,0} = \varepsilon_i / \ln[(b_i + \varepsilon_i)/a_i], \tag{11}$$

where $\varepsilon_i = (b_i^2 - a_i^2)^{1/2}$ and $b_i = \mathrm{AR}_i\ a_i$, with a_i and AR_i being determined as for snow (see above). Third, for the ventilation coefficients, instead of Eq. (3) we use formulae provided by Wang and Ji [1992; see Eqs. (13)–(90a,b,c) in PK97] for columns, plates, and dendrites, with χ evaluated as for snow.

b. Melting of graupel and hail

For graupel and hail, meltwater initially accumulates in the interior of the ice particle, soaking air spaces (except for particles with a bulk density >910 kg m^{-3}) (RH87). When all air spaces are filled up, meltwater begins to accumulate on the exterior of the particle.

The ice component of melting graupel and hail particles is assumed to be spherical of radius, a_i, with a volume enclosed by its outer surface of $V_i = m_i/\rho_i = (4/3)\pi a_i^3$. Here ρ_i is the bulk density of the ice only, not

including any meltwater. This bulk density is equal to the dry value and does not change during melting. Except for particles with a bulk density similar to that of pure solid ice (>910 kg m^{-3}), the meltwater initially accumulates inside the particle, soaking its air spaces. Only when all the air spaces are soaked does meltwater accumulate on the exterior of the particle. Aerodynamic molding of the exterior meltwater may then tend to reduce the fall speed.

The surface temperature is obtained iteratively, in a manner similar to Eq. (1):

$$T_s = \min\{T - [L_s D_v/(k_a R_v)][e_{\text{sat},i}(T_s)/T_s - e/T] f_v/f_h, T_0\}. \quad (12)$$

The terminal velocity, v_i, determines the Reynolds number:

$$N_{\text{Re}} = v_i(2a_d)\rho/\eta_a, \quad (13)$$

where a_d is the radius of the entire particle (including meltwater). The ventilation coefficients for vapor are

$$f_v = 2(1 + 0.108\chi^2), \quad \chi < 1.4, \quad \text{for} \quad N_{\text{Re}} < 250 \quad (14)$$
$$2(0.78 + 0.308\chi), \quad \chi > 1.4$$

$$f_v = 1 + 0.108\chi^2, \quad \chi < 1.4 \text{ for } 250 < N_{\text{Re}} < 6000 \quad (15)$$
$$0.78 + 0.308\chi, \quad \chi > 1.4$$

$$f_v = 0.76\chi/2 \quad \text{for} \quad 6000 < N_{\text{Re}} < 20\,000 \quad (16)$$

$$f_v = (0.57 + 9 \times 10^{-6} N_{\text{Re}})\chi/2 \quad \text{for} \quad N_{\text{Re}} > 20\,000, \quad (17)$$

where $\chi = N_{\text{Sc}}^{1/3} N_{\text{Re}}^{1/2}$. For determining the ventilation coefficient for heat, f_h, Eqs. (14)–(17) are applied again except with $\chi = N_{\text{Pr}}^{1/3} N_{\text{Re}}^{1/2}$, where $N_{\text{Pr}} = \eta_a c_p/k_a$, and c_p is the specific heat capacity of air at constant pressure.

When the surface temperature reaches 0°C($T_s = T_0$), melting starts:

$$dm_i = -dt(4\pi C_i/L_m)(k_a[T - T_0] f_h + (D_v L_e/R_v) f_v(e/T - e_{\text{sat},w}(T_0)/T_0)). \quad (18)$$

The capacitance is

$$C_i = a_d \quad \text{for} \quad N_{\text{Re}} < 6000 \quad (19)$$
$$a_i \quad \text{for} \quad N_{\text{Re}} > 6000.$$

If LWF > 0, then meltwater evaporates (condenses)

$$dm_w = -[dm_i L_m + dt(4\pi C_i f_h) k_a (T - T_0)]/L_e. \quad (20)$$

However, for LWF = 0, sublimation (vapor deposition) occurs [see Eq. (10)].

The volume occupied by all the meltwater is $V_w = m_w/\rho_L$. During melting, there is a soakable volume inside the ice core consisting of air and/or water (but not ice: see RH87) if the bulk density of the graupel or hail is appreciably less than that of pure ice. For very high-density particles with $\rho_i > 910$ kg m^{-3}, then $V_{\text{soakable}} = 0$, but for all other particles:

$$V_{\text{soakable}} = V_i - m_i/\rho_I. \quad (21)$$

Here, $\rho_I = 920$ kg m^{-3} is the density of pure ice. The smooth-sphere Reynolds number, $N_{\text{Re, smooth}}$, is a function only of the Best number:

$$X_{\text{Best}} = 8(m_i + m_w)\rho g/(\pi \eta_a^2). \quad (22)$$

This function is specified by RH87. There are two stages of melting corresponding to whether meltwater is on the exterior of the particle.

1) Soaking stage

During the soaking stage ($V_w < V_{\text{soakable}}$), meltwater is located only inside the ice core. The entire particle's radius is

$$a_d = a_i. \quad (23)$$

The dry Reynolds number, $N_{\text{Re,0}}$, is the hypothetical Reynolds number of the same particle if fully frozen:

$$N_{\text{Re, 0}} = v_{i,0}(2a_{i,0}\rho)/\eta_a, \quad (24)$$

where $a_{i,0} = \{[(m_i + m_w)/\rho_i]/(4\pi/3)\}^{1/3}$. The terminal velocity is

$$v_i = N_{\text{Re, smooth}}\eta_a/(2a_i\rho) \quad \text{for} \quad N_{\text{Re, 0}} < 4000 \quad (25)$$
$$v_{i,0}a_{i,0}/a_i \quad \text{for} \quad N_{\text{Re, 0}} > 4000.$$

The surface of the ice particle becomes wet as soon as melting begins. Consequently, for $N_{\text{Re,0}} < 4000$, the actual Reynolds number is assumed to be that of a smooth sphere ($N_{\text{Re,smooth}}$) of the same total mass as the particle. However, for high dry Reynolds numbers ($N_{\text{Re,0}} > 4000$), the smoothness of the particle surface is irrelevant: the actual Reynolds number and the drag coefficient are then assumed to be unchanged, being equivalent to those of the dry unmelted particle. Here, $a_{i,0}$ and a_i are the initial dry and current radii, while $v_{i,0}$ is the dry fall speed for a fully frozen particle of the same mass.

2) Fully soaked stage

During the fully soaked stage, ($V_w > V_{\text{soakable}}$), meltwater accumulates on the exterior of the ice corer and the entire particle's radius is

$$a_d = \{[V_i + (V_w - V_{\text{soakable}})]/(4\pi/3)\}^{1/3}. \quad (26)$$

The maximum mass of meltwater that can accumulate on the exterior of the particle is

$$m_{w,\mathrm{crit}} = 0.268 \times 10^{-3} + 0.1389(m_i + m_{w,\mathrm{soaked}}), \quad (27)$$

where $m_{w,\mathrm{soaked}} = \rho_L V_{\mathrm{soakable}}$.

The terminal velocity of the fully soaked particle is then interpolated between the just-soaked value, $\upsilon_{i,\mathrm{justsoaked}}$ and the hypothetical equilibrium value, $\upsilon_{i,\mathrm{eqm}}$, corresponding to this maximum amount of meltwater:

$$\upsilon_i = \upsilon_{i,\mathrm{start}} + (\upsilon_{i,\mathrm{eqm}} - \upsilon_{i,\mathrm{justsoaked}}) \times (m_w - m_{w,\mathrm{soaked}})/m_{w,\mathrm{crit}}. \quad (28)$$

This hypothetical equilibrium fall speed is

$$\upsilon_{i,\mathrm{eqm}} = \begin{cases} [1.5 \times 10^{-5} N_{\mathrm{Re,shed}}/(2a_{\mathrm{crit}})] \times (1.2/\rho)^{1/2} & \text{for} \quad 5000 < N_{\mathrm{Re,shed}} < 25\,000 \\ N_{\mathrm{Re,\,fast}}\eta_a/(2a_{\mathrm{crit}}\rho) & \text{for} \quad N_{\mathrm{Re,\,shed}} > 25000 \\ \upsilon_R & \text{for} \quad N_{\mathrm{Re,\,shed}} < 5000 \end{cases} \quad (29)$$

where

$$a_{\mathrm{crit}} = [(V_i + m_{w,\mathrm{crit}}/\rho_L)/(4\pi/3)]^{1/3}$$

and where

$$N_{\mathrm{Re,\,shed}} = 4800 + 4831.5(m_i + m_{w,\mathrm{soaked}}) \times 1000 \quad (30)$$

$$N_{\mathrm{Re,\,fast}} = (X_{\mathrm{Best,crit}}/0.6)^{1/2}. \quad (31)$$

For the very large particles with $N_{\mathrm{Re,shed}} > 25\,000$, the drag coefficient is 0.6. Here, the critical Best number is $X_{\mathrm{Best,crit}} = 8(m_i + m_{w,\mathrm{soaked}} + m_{w,\mathrm{crit}})\,\rho g/(\pi\eta_a^2)$.

The hypothetical just-soaked fall speed is

$$\upsilon_{i,\mathrm{start}} = \begin{cases} N_{\mathrm{Re,\,smooth}}\eta_a/(2a_{i,\mathrm{justsoaked}}\rho) & \text{if} \quad N_{\mathrm{Re},0} = \upsilon_{i,0}(2a_{i,0}\rho)/\eta_a < 4000 \\ & \text{or} \quad \rho_i < 800\ \mathrm{kg\ m^{-3}}; \\ \upsilon_{i,0}a_{i,0}/a_{i,\mathrm{justsoaked}}, & \text{otherwise.} \end{cases} \quad (32)$$

Here, when the particle was just soaked (i.e., at the beginning of the fully soaked stage), the radius of the particle was $a_{i,\mathrm{justsoaked}} = [(m_{i,\mathrm{justsoaked}}/\rho_i)/(4\pi/3)]^{1/3}$ and its mass of ice was

$$m_{i,\mathrm{justsoaked}} = (m_i + m_w)/(1.0 + \rho_L/\rho_i - \rho_L/\rho_I). \quad (33)$$

For particles with a high bulk density, $\rho_i > 910\ \mathrm{kg\ m^{-3}}$, then we apply the same formulas for $\upsilon_{i,\mathrm{start}}$ except with $a_{i,\mathrm{justsoaked}} = a_{i,0}$. Shedding of excess meltwater occurs whenever the mass of exterior meltwater exceeds an critical equilibrium value, $m_{w,\mathrm{crit}}$:

$$m_w - m_{w,\mathrm{soaked}} > m_{w,\mathrm{crit}}. \quad (34)$$

Shed drops have a size that is dependent on the particle's Reynolds number (Rasmussen et al. 1984b). For $N_{\mathrm{Re}} = \upsilon_i(2a_d)\rho/\eta_a > 25\,000$, all exterior meltwater is shed discontinuously as a burst of raindrops of 1.5 mm in diameter when its mass exceeds the critical threshold. For $15000 < N_{\mathrm{Re}} < 25\,000$, there is continuous shedding of such raindrops and the mass of exterior meltwater is maintained at exactly the critical equilibrium value. For $N_{\mathrm{Re}} < 15\,000$, there is intermittent shedding of raindrops of 3 mm ($N_{\mathrm{Re}} > 10\,000$) or 4.5 mm ($N_{\mathrm{Re}} < 10\,000$) in diameter, reducing the mass of exterior meltwater in each shedding event such that it is less than $m_{w,\mathrm{crit}}$. The mass of meltwater that is shed in any such event may not exceed a prescribed fraction (50%) of $m_{w,\mathrm{crit}}$.

c. Design of numerical experiments

We present below results from simulations of deep convective clouds in environments characterized by various thermodynamical conditions with different aerosol (CCN) properties. In all simulations, the computational area was 128 km × 16 km while the resolution was 250 and 125 m in the horizontal and vertical directions, respectively. For calculation of the initial (at $t = 0$) CCN size distribution, an empirical dependence (PK97) was applied:

$$N = N_o S_w^k, \quad (35)$$

where N_0 and k are measured constants, and S_w is the supersaturation with repect to water (in %). The procedure for evaluation of the size of activated CCN and nucleated droplets is described by Khain et al. (2000). At $t > 0$ the prognostic equation for the size distribution function of nonactivated CCN is solved. Using the value of S_w calculated at each time step, a critical CCN radius is calculated according to Kohler theory. Those CCN with radii exceeding the critical value are activated (new droplets are nucleated). Corresponding bins of the CCN size distributions then become empty. Aerosol particles are assumed to be soluble. The maximum size of dry aerosol particles is assumed to be 1 μm, which corresponds to a radius of ~4 μm for a newly nucleated droplet. Effects of giant CCN are not considered in the present study.

To illustrate the effects of detailed melting on deep convective clouds arising under maritime thermodynamic conditions, we simulated clouds using profiles from the 1200 UTC sounding on board the Canadian ship *Quadra* on 18 September 1974 of the GATE experiment. This sounding has been used in many previous modeling studies of maritime convection (e.g.,

Turpeinen and Yau 1981; Ferrier and Houze 1989; Khain et al. 2004). The maritime aerosol distribution was characterized by parameters, $N_0 = 100$ cm^{-3} and $k = 0.462$ in Eq. (35). Additionally, in accordance with measurements made by Hudson (1993), it was assumed that there were no small CCN that could be activated at supersaturations exceeding 1.0%.

The differential effect of melting schemes on the dynamics and microphysics of convective clouds developing over the land was investigated using several case studies with various thermodynamic and aerosol conditions: (i) in Texas on 13 August 1999 (Rosenfeld and Woodley 2000); (ii) green-ocean, smoky, and pyro-clouds observed over Amazon by a research aircraft during the LBA–SMOCC campaign at 1900 UTC 1 October 2002 (10°S, 62°W) and 1900 UTC 4 October (10°S, 67°W) (Andreae et al. 2004). The Texas environmental conditions (Khain et al. 2001) reveal a significant convective instability of the atmosphere. The surface temperature was as high as 36°C, and the surface relative humidity was about 35%. The freezing level was at 4.5 km above the surface. Parameters N_0 and k were set equal to 1260 cm^{-3} and 0.308, respectively (Khain et al. 2001; Khain and Pokrovsky 2004). The CCN size distribution was truncated at $r_N = 0.5$ μm. This cutoff radius corresponds to a radius of newly nucleated droplets of about 2.5 μm.

Thermodynamic conditions in green-ocean, smoky, and pyro-clouds were quite similar. Based on the measurements (Roberts et al. 2002; Rissler et al. 2004; Martins et al. 2004), parameters N_0 and k were set equal to 255 cm^{-3} and 0.97 for simulations of green-ocean clouds, and to 3670 cm^{-3} and 0.897 for simulations of smoky clouds. Detailed calculations of the surface heat and aerosol fluxes from the surface within the zone of forest fire are beyond the scope of the study. Instead, we have assumed that the initial concentration of aerosol particles in the boundary layer is similar to that of the smoky cloud. Within the region of biomass burning (2 km in width, 250 m in depth) the CCN concentration was assumed to be twice as large. In all simulations, the initial aerosol concentration was assumed to be constant up to $z = 1.5$ km, exponentially decreasing with height above this level. A characteristic height-scale of 2 km is applied for this exponential fall-off (Martins et al. 2004). As a result, maximum droplet concentrations simulated in these clouds varied from ~500 cm^{-3} in green-ocean cloud up to ~2500 cm^{-3} (smoky cloud) and 2700–4000 cm^{-3} (pyro-cloud), which is in a good agreement with measurements (Andreae et al. 2004).

In simulations of maritime (GATE), Texan, green-ocean, and smoky clouds, the formation of cloud was triggered by an initial pulse of heating in the boundary layer lasting 10 min, at the center of the computational area ($x = 64$ km, where x is the horizontal distance from the edge of the domain). The maximum heating rate was 0.03°C s^{-1} in the center of the 5 km × 2 km heating area. In pyro-cloud simulations, convection was triggered and sustained by a continuous heating within the region of 2 km width and 2 km depth. The maximum intensity of this heating (0.25°C s^{-1}) was chosen so as to allow the simulated pyro-clouds to reach the observed cloud-top height of ~12 km. Moreover, the surface temperature in the fire zone was assumed to be 100°C. These conditions allowed us to simulate strong cloud with a realistic depth and a maximum vertical velocity of about 40 m s^{-1} that is typical of pyro-clouds observed in the region. Most simulations were performed for time periods of a few hours. Hence, there was no need to account for any motion of the heating zone. At the surface, the temperature and water vapor mixing ratio were assumed to remain unchanged during the simulations.

3. Results: Overview of maritime and continental cases

Figures 1 and 2 depict the vertical profiles of latent heating, averaged over time and horizontally, and the accumulated rain at the surface for the maritime case from GATE and the two continental cases of deep convection. The heating is caused by condensation, freezing, and deposition. The cooling is caused by droplet evaporation, ice sublimation, and melting. Net heating represents the sum of latent heating and cooling. Figure 1 shows that in the maritime case (and also in the green-ocean cloud case, see below), the differences between latent heating/cooling profiles from simulations with and without the detailed melting scheme are much smaller than in the continental cases. In particular, the extra cooling in the melting layer due to detailed melting is less than in the continental cases and produces less impact both on the convective instability and on downdrafts causing the low-level horizontal convergence (see mechanisms 1 and 2 in section 1). Consequently, the difference in accumulated rain amount at the surface is reatively low (see Fig. 2a). This result may be attributed to the following. First, in the case of low CCN concentrations (as in the maritime and green-ocean cloud cases), the dominant fraction of total precipitation is from the warm rain process (e.g., Khain and Pokrovsky 2004). Effects related to ice processes, including melting, are therefore less important. Second, larger precipitating particles form in these maritime/green-ocean clouds at lower altitudes, owing to faster growth of droplets by condensation and more efficient

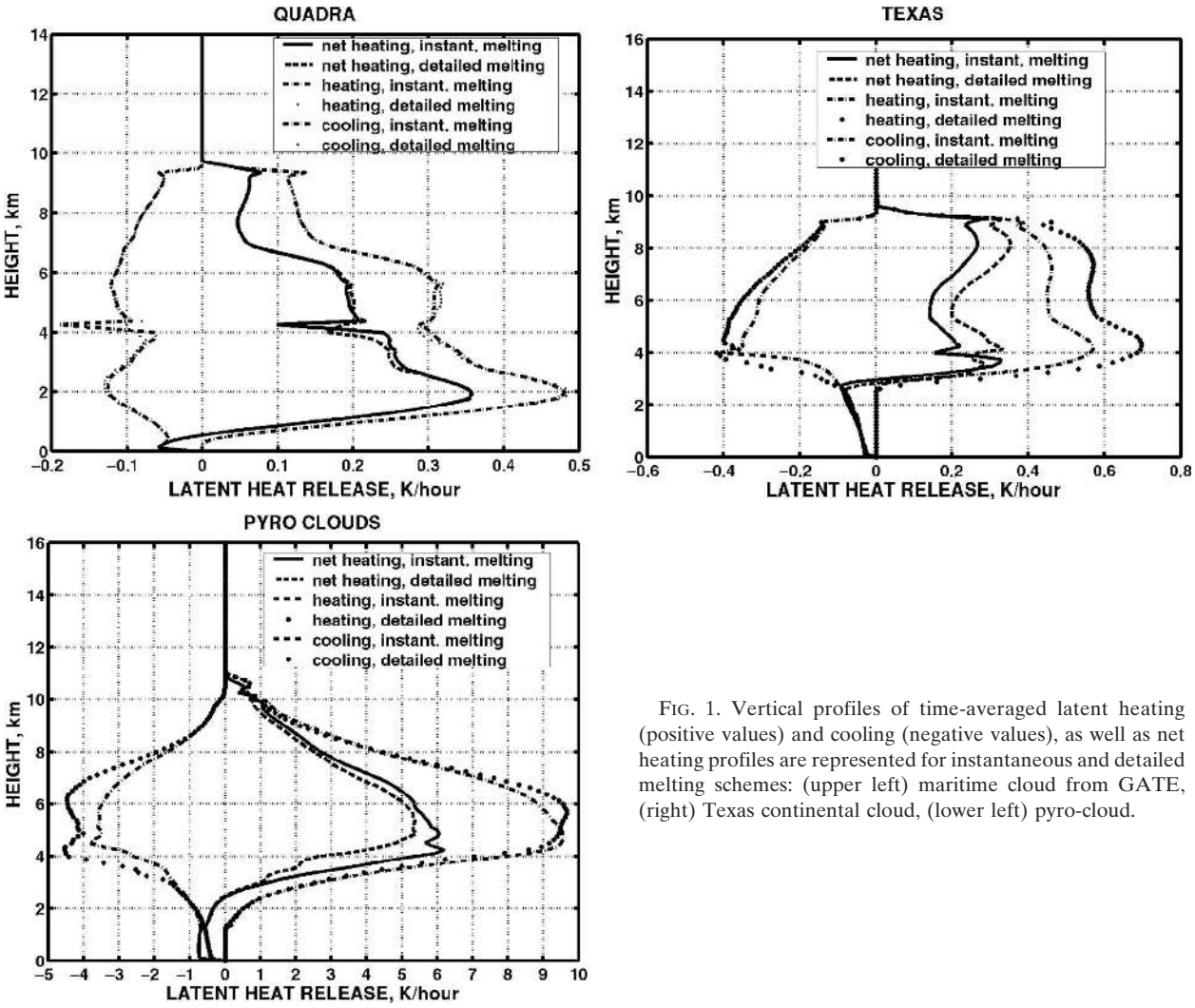

FIG. 1. Vertical profiles of time-averaged latent heating (positive values) and cooling (negative values), as well as net heating profiles are represented for instantaneous and detailed melting schemes: (upper left) maritime cloud from GATE, (right) Texas continental cloud, (lower left) pyro-cloud.

collisions. As a result, the precipitating particles (including large graupel and hail) fall through, or near, cloudy updrafts without creating horizontal temperature gradients and without intensifying downdrafts. The situation changes (see below) for continental clouds with high CCN concentration. In previous studies, horizontal temperature gradients from melting-induced latent cooling have been found to be important for accelerating downdrafts (Szyrmer and Zawadzki 1999) and for causing mesoscale oscillations of the horizontal wind (Atlas et al. 1969).

Figure 2 shows opposite responses of accumulated surface precipitation when detailed melting is included, between the Texas and pyro-cloud cases. These are explicable as follows. Secondary convective cells form in the Texas case with detailed melting, increasing the accumulated surface rainfall. Losses of cloud ice by sublimation in the environment are higher in the pyro-cloud case with detailed melting (see section 6) than with instantaneous melting, because the updrafts are more vigorous.

Figure 3 depicts vertical profiles of equivalent potential temperature, with which the consequences from the choice of melting scheme on the convective instability of the local atmosphere may be assessed (see mechanism 2 in section 1). These profiles are conditionally averaged over all regions where the total ice content (IWC) > 1 g m^{-3} (IWC includes both cloud ice and ice precipitation) at the first model level above the freezing level, over the entire duration of simulations of the maritime, Texas, and pyro-cloud cases. In the maritime and Texas cases, the changes of average temperature caused by implementation of the detailed melting scheme are quite small, probably because of the relatively low amount of ice falling through the freezing level. Nevertheless, in both of these cases, the minimum

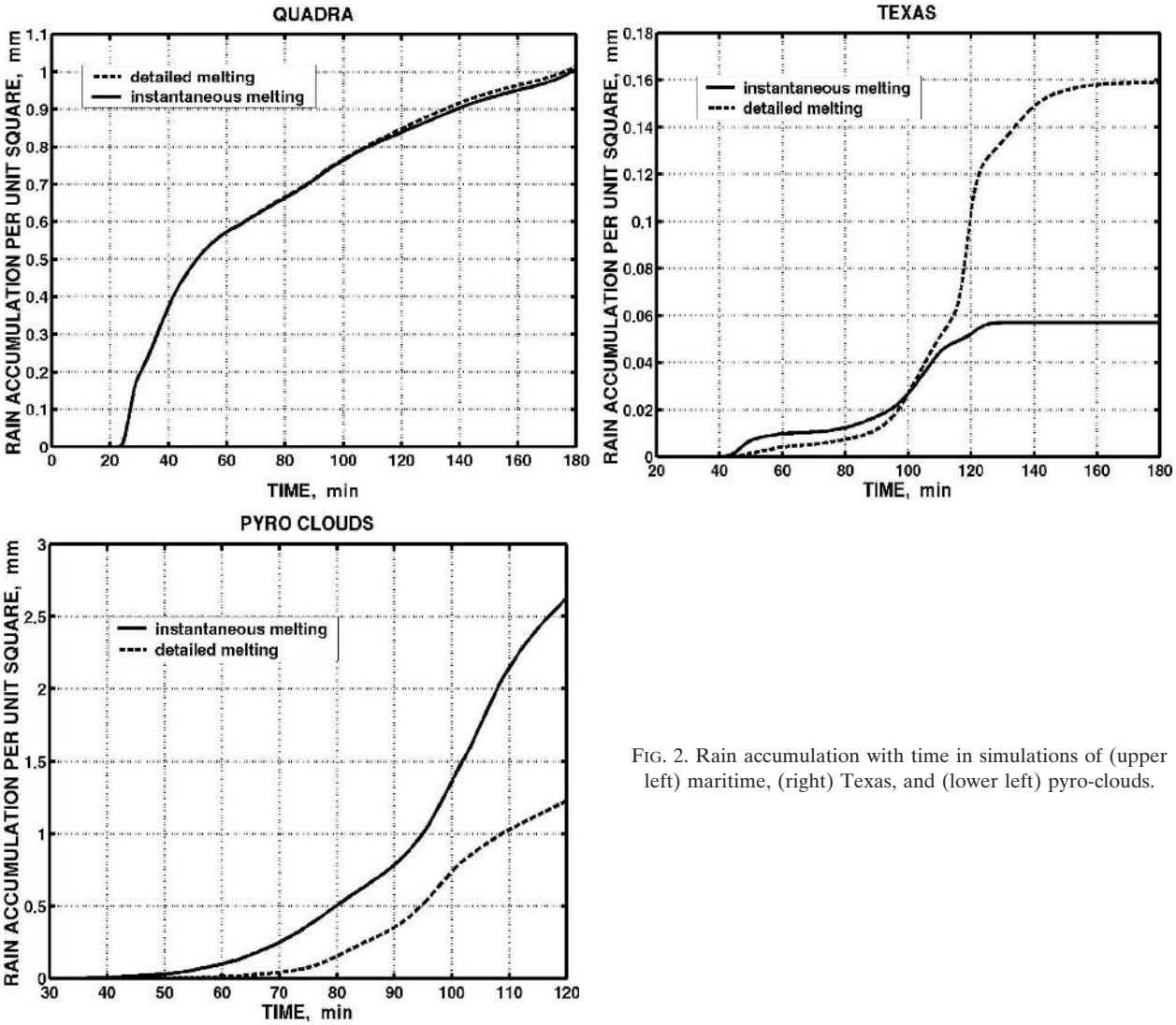

FIG. 2. Rain accumulation with time in simulations of (upper left) maritime, (right) Texas, and (lower left) pyro-clouds.

of equivalent potential temperature in the case of instantaneous melting just below the freezing level is less intense, or absent, in the case of detailed melting. In particular, the discontinuity there disappears.

By contrast, in the pyro-cloud case, the sensitivity of average equivalent potential temperature is much higher, with this minimum just below the freezing level being intensified by inclusion of detailed melting due to extra melting-induced latent cooling noted above. This extra latent cooling is partly caused by prolonged periods of sublimation, and evaporation of meltwater, of ice particles below the freezing level (melting particles fall more slowly than raindrops of the same mass) in the case of detailed melting (see section 6). Such cooling in the lower troposphere in zones of melting—typically in downdrafts—destabilizes the lower troposphere at 3–4 km MSL with respect to convection in stratiform cloud by steepening the lapse rate of equivalent potential temperature, which acts to invigorate convective motions (mechanism 2 in section 1). The extra latent cooling must also intensify downdrafts in deep convective cloud, which increases the low-level convergence yielding more vigorous updrafts of deep convection (mechanism 1 in section 1) in the pyro-cloud case when detailed melting is included (see section 5b).

4. Results: Maritime simulations with detailed melting scheme

Despite small effects on the precipitation amount, simulations of the GATE maritime case (18 September 1974) reveal modest, yet significant, changes of the cloud microphysics when the detailed melting scheme is included. During this case, which lasts 3 h, there is one

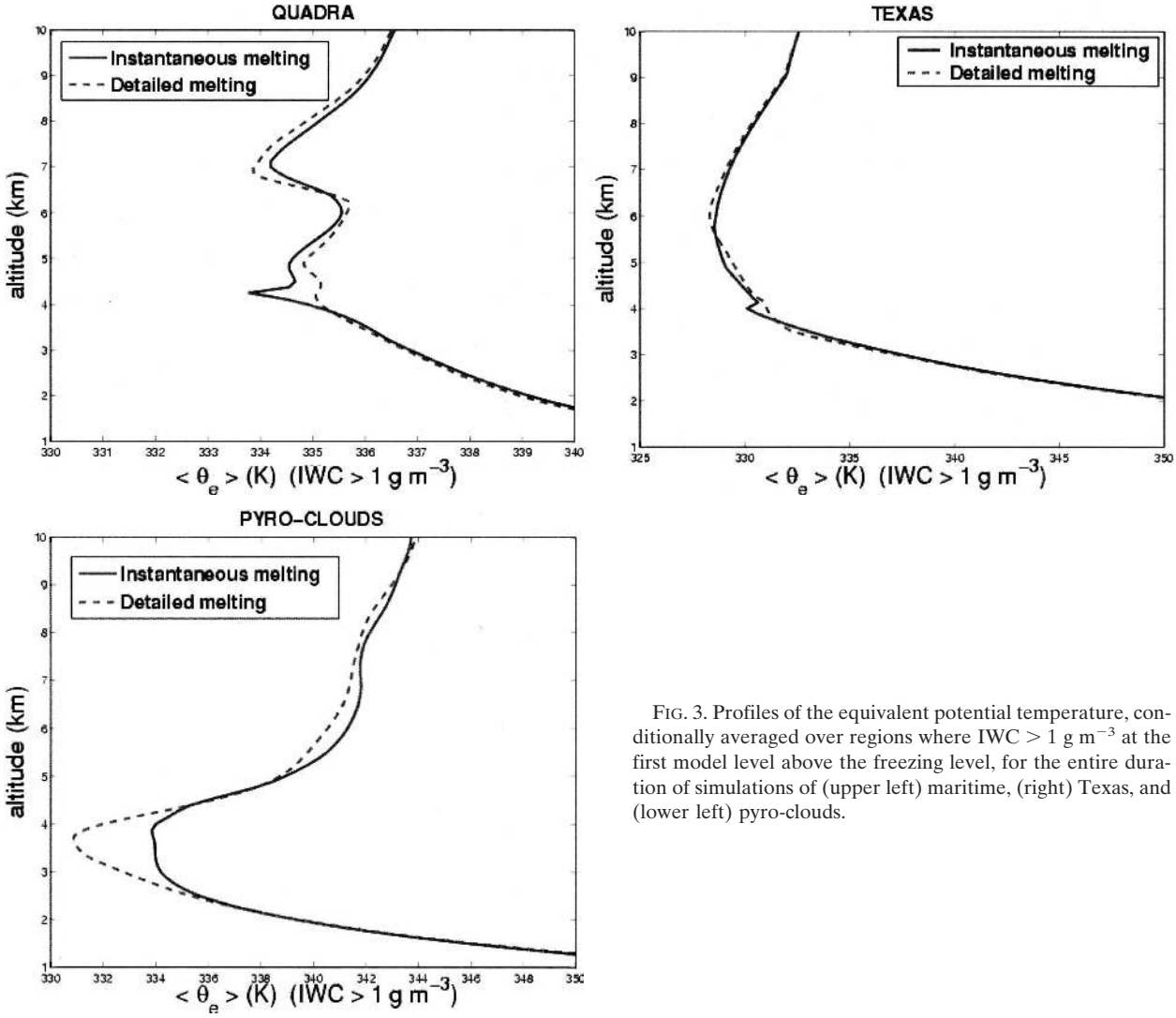

FIG. 3. Profiles of the equivalent potential temperature, conditionally averaged over regions where IWC > 1 g m^{-3} at the first model level above the freezing level, for the entire duration of simulations of (upper left) maritime, (right) Texas, and (lower left) pyro-clouds.

ascending updraft bubble with maximum values of vertical air velocity and of cloud content that lifts the cloud-top level up to 12 km MSL. The average updraft speed in this bubble is about 3 m s^{-1} when it is below the freezing level, attaining values of up to 8 m s^{-1} later above 7 km MSL. This deep updraft produces copious graupel, which falls out and melts, causing two episodes of intense rain-out at $t = 60$ min and 105 min. Generally, the mass of hail is almost negligible during the entire simulation, except within a layer that is about 200–300 m deep near the freezing level, where hail is formed by the riming of graupel within the range of $-3°$ to 0°C (see Khain et al. 2004). Primary ice nucleation and freezing of cloud droplets aloft yield crystals and frozen droplets in the updraft above 7 km MSL. Crystals are detrained into an anvil at about 9–12 km MSL, where they may eventually aggregate to form snow. This snow falls out slowly and does not appear to contribute to the main precipitation episodes at the surface. Following the arrival of rain near the surface from the main bubble, secondary clouds with cloud tops below 3 km MSL are formed. The average updraft speed in these secondary clouds is mostly almost 3 m s^{-1}. However, these secondary clouds are weak in the maritime case and do not develop.

Figure 4 demonstrates an increase in cloud liquid and cloud ice contents, which are plotted here as domain averages. Such changes caused by the inclusion of detailed melting are of the order of 1%–10% and represent actual increases within clouds (rather than offsets of maxima with respect to altitude or time). Greatest percentage differences are seen in the anvil above 10 km MSL for cloud ice and near or below the melting layer for cloud liquid. Note that the cloud base of the

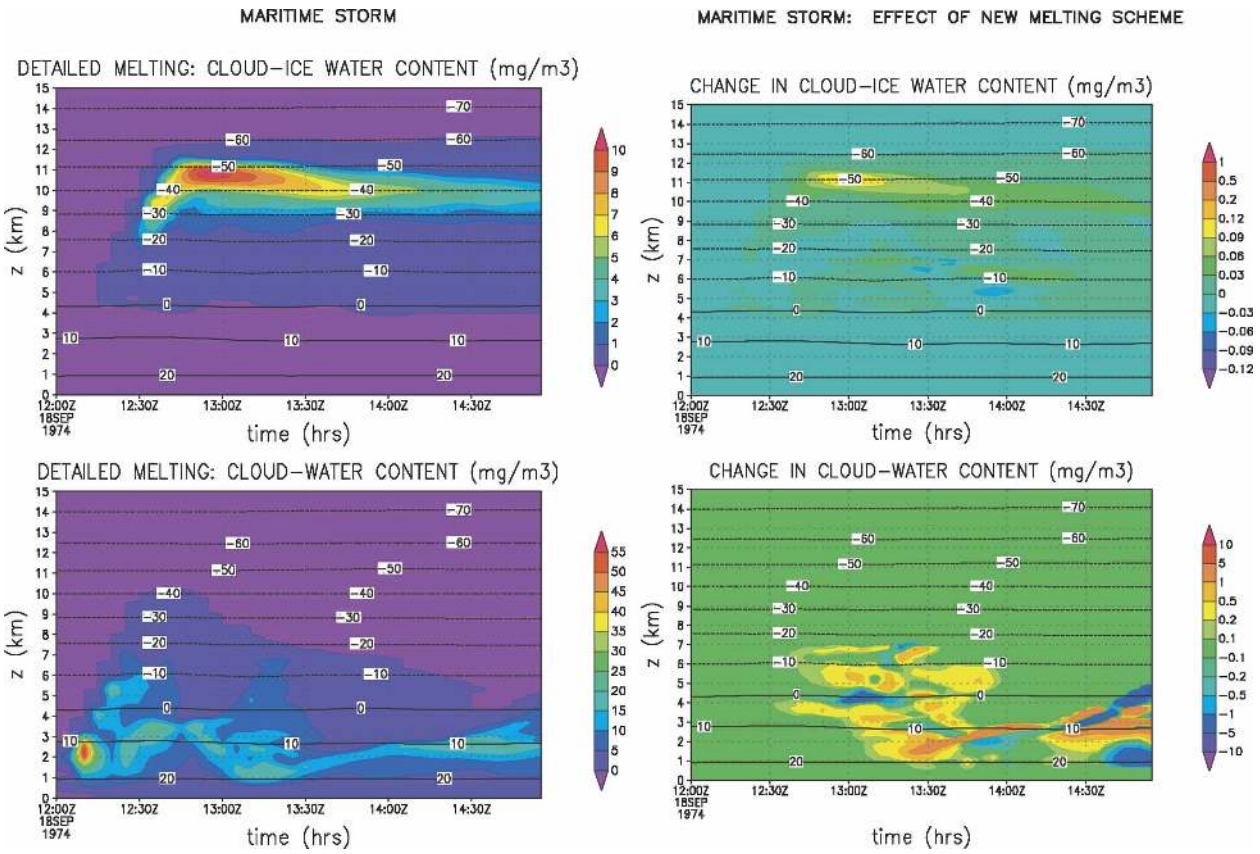

FIG. 4. (left) Cloud ice and cloud liquid contents, domain-averaged at all levels, for the maritime GATE simulation in the case of detailed melting. (right) The difference between detailed melting and instantaneous melting is shown, depicting the effect of inclusion of the detailed melting scheme.

deep convection is located at about 1 km MSL, which is at least 3 km lower than the freezing level. Figures 5 and 6 indicate a significant increase in graupel and hail contents of about 1%–10% above the freezing level when the detailed melting scheme is included. This enhancement of the mass of ice aloft is caused by convection being slightly invigorated, with the main updraft being faster by up to about 1 m s^{-1} and upwelling ice particles to higher levels (see Fig. 6). Consequently, cloud contents are larger above the freezing level in the detailed melting case. Slight increases in updraft speeds are caused by more intense rates of melting-induced latent cooling in the case of detailed melting. This boosts downdrafts, intensifies low-level convergence and modifies ambient temperature profiles of the local environment in the vicinity of deep convection.

Difference maps in Figs. 5 and 6 portray the tangible effect on the vertical distribution of ice mass below the freezing level when detailed melting is included (no ice in the instantaneous melting case exists there). For snow, graupel, and cloud ice, most of their mass melts over the 300-m layer just below the freezing level in the detailed melting maritime case (at least 90% for the graupel). For hail, about half of its mass melts over this distance. A small fraction (<1% for graupel, about 5% for hail) of the ice mass penetrates down to levels more than 1 km below the freezing level. Thus, the distance of complete melting is much larger than the distance for melting of most of the ice mass. This small fraction corresponds to the few largest particles that require a very long time to melt. Hail mass is found to penetrate much further toward the surface after falling through the melting level than other ice species in the case of detailed melting.

5. Results: Simulations of continental clouds

a. Summertime Texas clouds

Simulations of Texas continental clouds reveal significant differences in the results obtained using different melting schemes. Firstly, in the case of high CCN concentrations, the droplet concentration is high and the average size of droplets is reduced. As a result, droplets reach higher levels and are more likely to

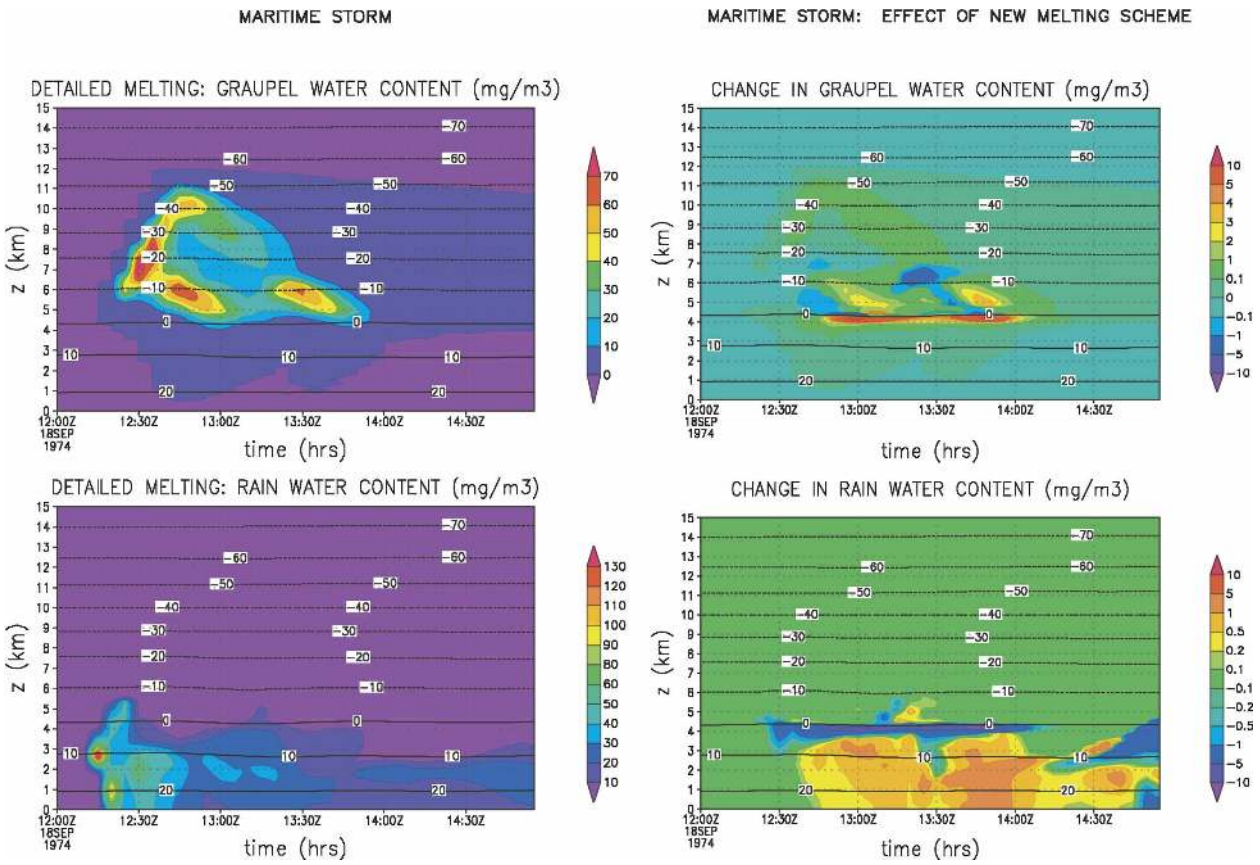

FIG. 5. Graupel and rain contents, plotted as in Fig. 4.

freeze. Hence, the ice precipitation, which falls out slowly downshear from cloudy updrafts, dominates the overall precipitation from these clouds. This fact does not by itself explain the difference between results obtained using both melting schemes; rather, it explains why ice processes play a crucial role in the evolution of these continental clouds, so that changing the melting scheme can influence their cloud microphysics and dynamics.

The physical mechanism for destabilization of the troposphere by ice melting is illustrated in Fig. 7, where fields of vertical velocity and total ice content are shown at $t = 6300$ s, a time from the simulation when deep convection is particularly intense. In the case of detailed melting, most of the mass of ice melts over a narrow layer just below the freezing level that is a few hundred meters deep, as was found in the maritime case (see section 4), while a small fraction of the ice melts over a much deeper layer than this of up to 1.5–2 km in depth. Inclusion of the detailed melting scheme is found to cause stronger latent cooling, mostly between the freezing level and 3 km MSL (see Fig. 1b) and faster downdrafts in the area of ice melting, relative to the instantaneous melting scheme. Such downdrafts penetrate into the lower layer below 1–2 km MSL. Latent cooling caused by sublimation and melting of ice, and by evaporation of meltwater on melting ice, plays an important role in enhancing the horizontal vorticity associated with updraft–downdraft pairs. Consequently, in the simulation with detailed melting included, a new cloud cell arises from the BL, as shown in Fig. 7. In the case of instantaneous melting, the corresponding secondary cloud cell is too weak and does not develop during the model integration.

Figure 2b shows that the amount of accumulated rain is 2.5 times larger in the detailed melting case than in the case of instantaneous melting. This is mainly because of the formation of the secondary clouds in the case of detailed melting. Note, however, that in any case, precipitation from Texas clouds is significantly smaller than in the case of maritime convection.

b. Green-ocean, smoky, and pyro-clouds in the Amazon region

Simulations of clouds under different CCN concentrations (green-ocean, smoky, and pyro-clouds) ob-

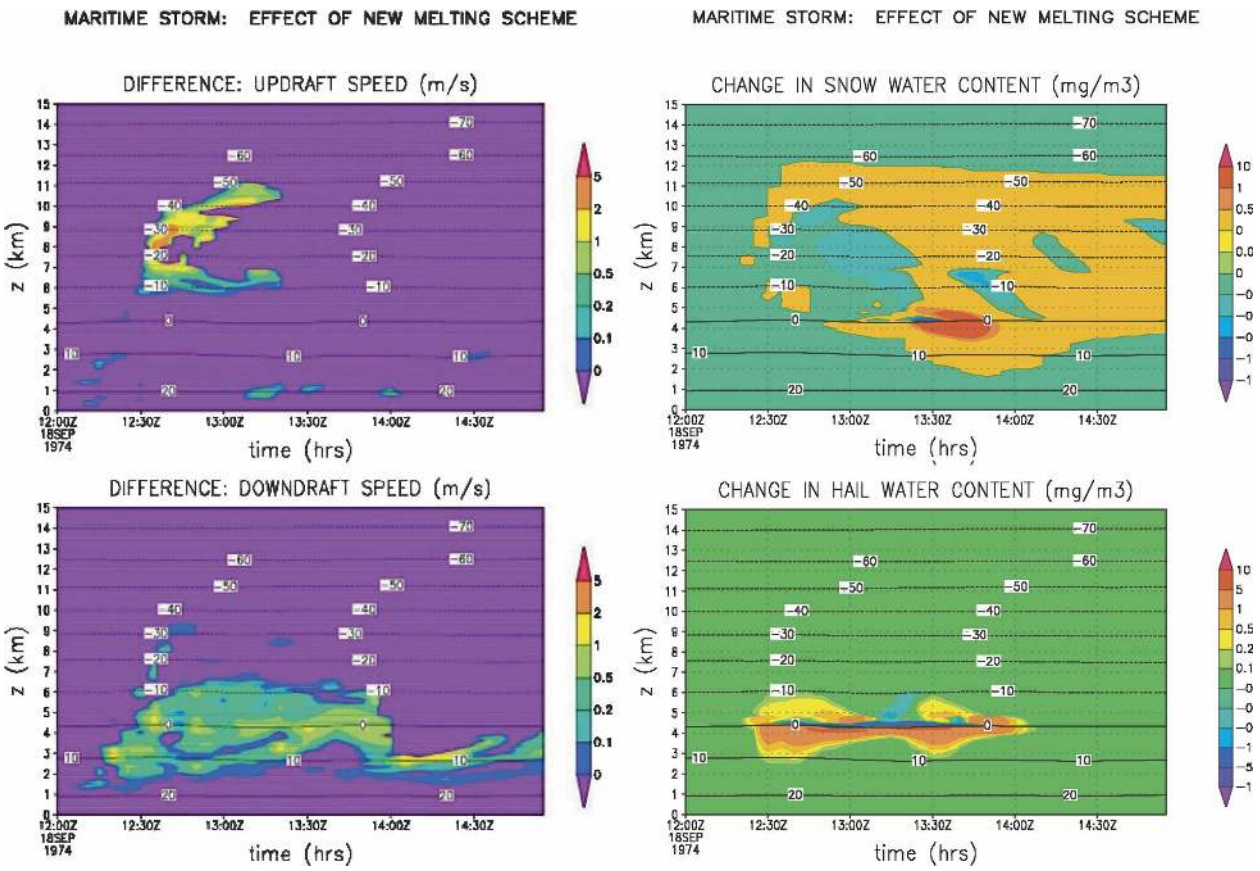

FIG. 6. Changes in updraft and downdraft speeds (conditionally averaged over cloudy regions), and in snow and hail contents, when detailed melting is included.

served during the LBA–SMOCC campaign on 1900 UTC 1 October 2002 (10°S, 62°W) and 1900 UTC 4 October (10°S, 67°W) (Andreae et al. 2004) support conclusions reached in the analysis of maritime and very continental cases discussed above. No significant sensitivity of the surface precipitation was found for the green-ocean cloud, with respect to the choice of melting representation. This behavior is similar to that found in the maritime simulation (see section 5a), which has an environmental CCN concentration similar to that prescribed in the green-ocean case (see section 2c). Both with and without the detailed melting scheme, accumulated rain amounts after 2 h of cloud evolution were about 0.7 mm (not shown). This is 1.5 times less than in the maritime clouds simulated in the present study.

Simulations of smoky and, especially, pyro-clouds all indicate that inclusion of detailed melting invigorates convection. Effects from inclusion of the detailed melting scheme on the structure of smoky cloud are illustrated in Figs. 8 and 9. Figure 8 compares fields of total ice content (the sum of all ice species) and of rainwater content at $t = 3900$ s in simulations of the smoky cloud with the detailed melting (left panels) and instantaneous melting (right panels) schemes. One can see that the total ice content is larger and ice penetrates to higher levels in the case of the detailed melting relative to the instantaneous melting case. In both cases, precipitation is caused mainly by melting, while the structure of rainwater content (RWC) is quite different between them. In the case of instantaneous melting, the maximum in RWC is located just below the freezing level while in the detailed melting continental case it is located near the surface. This is because melting occurs over a layer of finite depth below the freezing level in the detailed melting case, as in the real atmosphere.

Figure 9 shows fields of aggregates (snow), graupel, and hail (upper panels), with corresponding fields of averaged (over all mass bins) LWF, for the case of detailed melting. Such liquid fractions indicate fractions of melted water contained in the corresponding ice species. Snow melts over the shortest vertical distance (penetration into the area of positive temperature layer

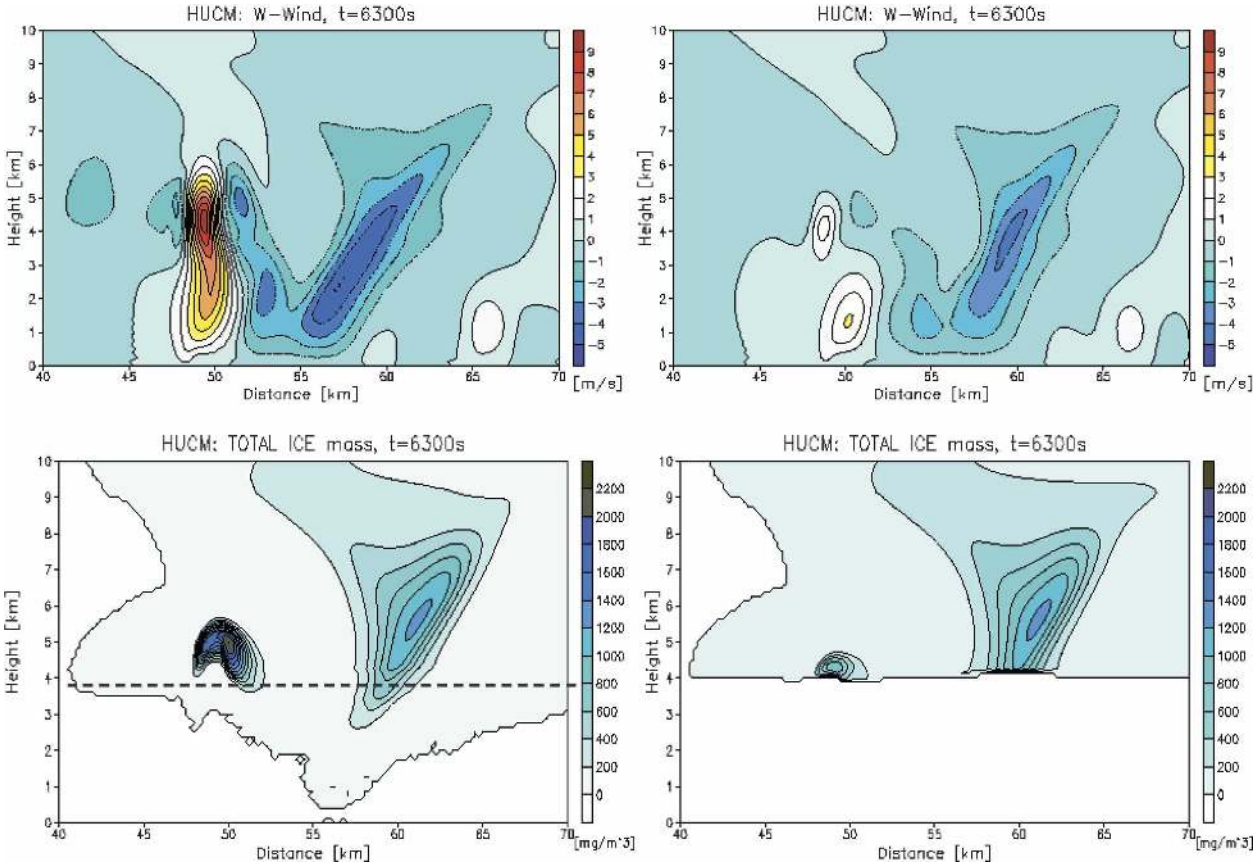

FIG. 7. Vertical velocity in simulations of Texan cloud at $t = 6300$ s using (upper left) the detailed melting scheme and (upper right) instantaneous melting. Also shown is the total ice content in simulations of Texas cloud at $t = 6300$ s using (lower left) the detailed melting scheme and (lower right) instantaneous melting. The height of the freezing level is indicated with a dashed line. The new cell that develops only in the detailed melting case is located at (left) about 48 to 50 km of horizontal distance, x. It is caused by downdrafts from the previous clouds at $x = 55$ to 65 km.

is about 500–700 m) out of these three ice precipitation species, while the largest particles of graupel and hail penetrate downward by about 1.5 km.

Effects of detailed melting on the structure of the pyro-cloud are illustrated in Figs. 10–11. Figure 10 shows that inclusion of the detailed melting scheme leads to formation of cloud that is convectively more vigorous, penetrating to higher levels. In the detailed melting case, vertical updrafts remain intense (>15 m s^{-1}) up to $z = 12$ km, while at the same time in the case of instantaneous melting the updrafts at upper levels do not exceed 5 m s^{-1}. The most intense downdrafts reach vertical speeds of 10 m s^{-1} in the case of instantaneous melting but attain 15 m s^{-1} in the case of detailed melting. Note that the difference in structure of the latent cooling caused by differences in the choice of melting scheme leads to different tilts of the updraft zones: they actually have an almost vertical structure in the case of detailed melting, whereas they are much more sloped in the instantaneous melting simulation. Figure 11 shows various fields in the pyro-cloud of different ice species, together with corresponding fields of averaged LWF in the simulation with detailed melting. Spatial separation of different ice species is evident: snow falls at a much larger distance downwind of the cloudy updraft than hail and newly formed graupel. Again, most of the mass of ice is found to melt quite rapidly within a few hundred meters below the freezing level, while a limited fraction of the ice mass (larger particles) penetrates significantly toward the surface. Spatial variability in the height of the freezing level is evident in Fig. 11, arising from variability in the spatial distribution of melting ice and its associated latent cooling. To illustrate the process of melting, Fig. 12 displays the size distributions of snow, graupel and hail, with respect to their mass concentration and LWF at various levels. These distributions are sampled from cross sections through regions of typical penetration of these species downward below the freezing level. The process of melting is found to start with the smaller particles in

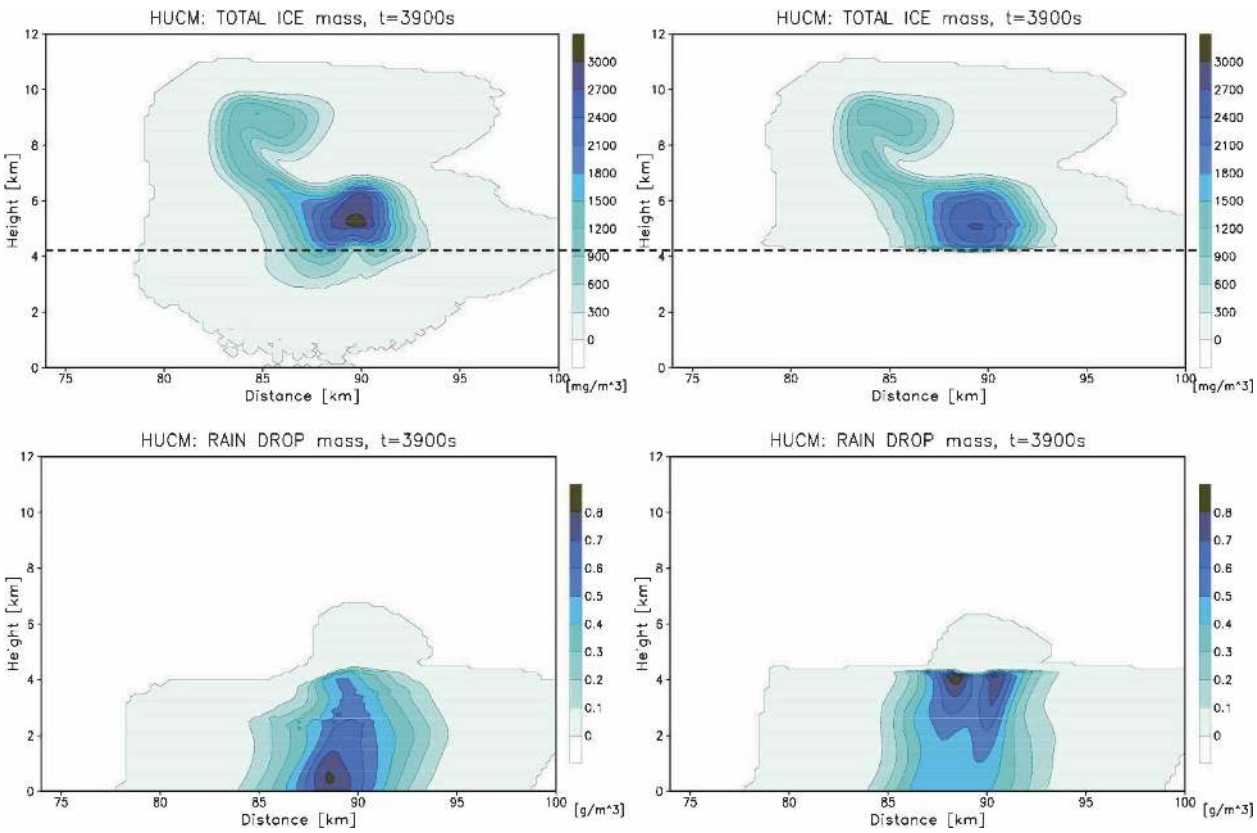

FIG. 8. (upper) Total ice and (lower) RWC in case of (left) detailed melting and (right) instantaneous mixing for the smoky cloud observed in LBA–SMOCC. The height of the freezing level is indicated with a dashed line.

the size distribution, so that at lower levels only the largest ones remain.

6. Summary and conclusions

Effects from latent cooling caused by the melting of ice that penetrates to levels below the freezing level are investigated using a spectral (i.e., with size bins) microphysics model that has a new detailed melting scheme. This melting scheme also is based on a spectral approach. Ice particles (graupel, hail, and snowflakes) are characterized by their size and a liquid fraction, LWF. The LWF, which is calculated for each mass bin, increases during the melting process from zero at (and above) the freezing level to unity (fully melted) at levels below it. Both ice size distributions and water fraction within each mass bin are calculated in the course of the model integration. This detailed melting scheme permits a very accurate simulation of the rate of melting of individual ice particles. The variations in terminal velocity due to evolution of the shape of particles during melting, with meltwater being molded by the aerodynamic airflow, are represented in this scheme, in contrast with previous modeling studies about the effects from melting.

Numerical simulations are performed of convective clouds developing under different thermodynamical and aerosol conditions (ranging from maritime clouds observed in GATE-74 over the Atlantic Ocean to pyroclouds observed in a region of forest fires in the Amazon). Results obtained from using the detailed melting scheme are compared with those from simulations with instantaneous melting at the freezing level (0°C).

Some general features commonly observed in zones of melting ice in stratiform clouds are reproduced qualitatively by the model with the detailed melting scheme. Such features, seen in aircraft observations of stratiform melting layers by Stewart et al. (1984) and Willis and Heymsfield (1989), include

- a narrow layer that is only a few hundred meters deep, over which most of the mass of ice melts, just below the freezing level;
- a layer of complete melting that is much deeper than this, extending down to 1–2 km below the freezing level;

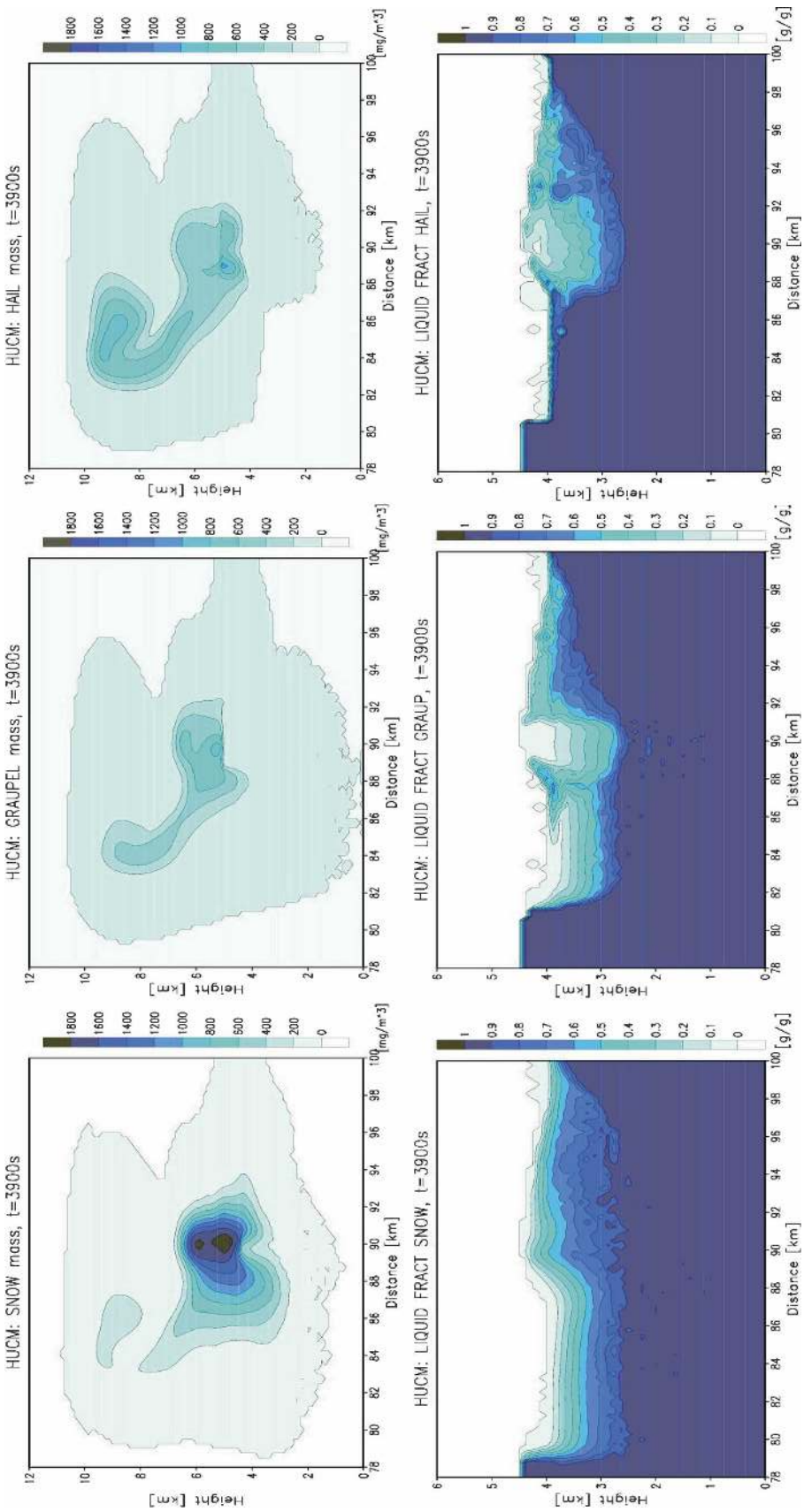

FIG. 9. Mass contents and averaged (over all mass bins) LWF fields at $t = 3900$ s, in the case of smoky cloud from LBA–SMOCC, for snow, graupel, and hail.

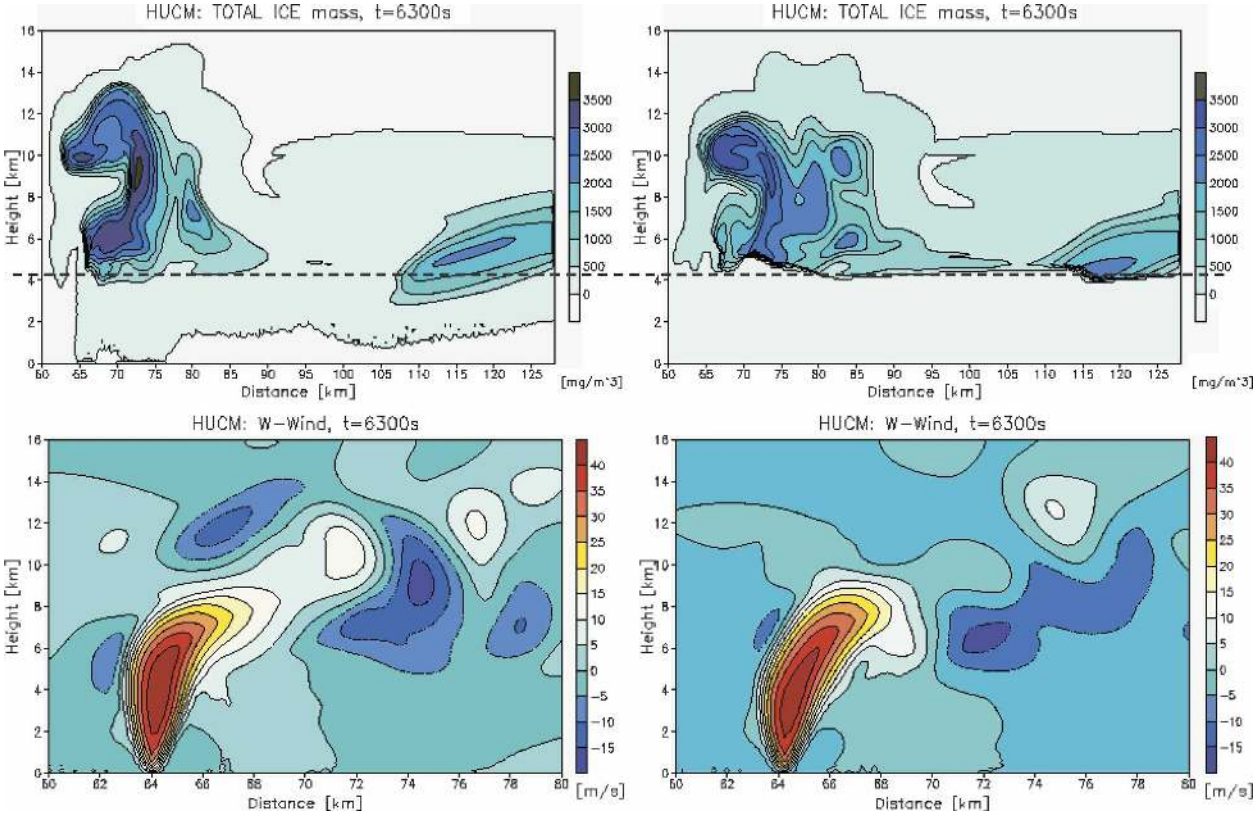

FIG. 10. Fields of (upper) total ice content and (lower) vertical velocity in simulated pyro-cloud at $t = 6300$ s in simulations with (left) detailed melting and the instantaneous melting. The height of the freezing level is indicated with a dashed line.

- a minimum in equivalent potential temperature at the base of this narrow layer over which most of the mass of ice melts (see Stewart et al. 1984), reflecting a tendency for the local lapse rate of physical temperature to be reduced within this layer as a result of melting-induced latent cooling.

In the simulations presented here, a sensitivity of the equivalent potential temperature profiles to the manner of representation of melting is found in regions of melting. This reflects the type of convective destabilization associated with steepening of lapse rates below the isothermal layer, as first described by Findeisen (1940) and modeled by Moore and Stewart (1985; see also Knight et al. 2004). However, among the simulations presented here, this type of destabilization of the lower troposphere is only found to be very pronounced in the pyro-cloud case.

It is the strengthening of downdrafts by enhanced rates of melting-induced latent cooling that constitutes the dominant mechanism by which melting influences deep convective clouds in simulations presented here. Downdrafts intensified by melting act to increase the horizontal convergence in the boundary layer, which intensifies convective updrafts. This mechanism for invigoration of moist convection is consistent with the findings of other previous studies (see mechanism 1 of the introduction): (i) melting-induced descent makes the primary contribution to formation of the cold pool at the surface in simulations of squall-type deep convection by Liu et al. (1997) and of rainbands by Barth and Parsons (1996; see section 1); and (ii) intensification of updrafts can result from the lower-level convergence created by this descent impinging on the surface, in simulations by Szeto and Stewart (1997).

The latent cooling, simulated when the detailed melting scheme is included, is more intense than in corresponding cases of instantaneous melting (see section 3). It is also more realistic. Such higher rates of latent cooling are explicable as follows. First, melting particles fall more slowly than raindrops of the same mass. Hence, the duration of the period of latent cooling by evaporation of meltwater (and prior sublimation) is more prolonged during their fallout in cases of detailed melting, compared to the period of evaporation of raindrops of the same mass in corresponding cases of instanta-

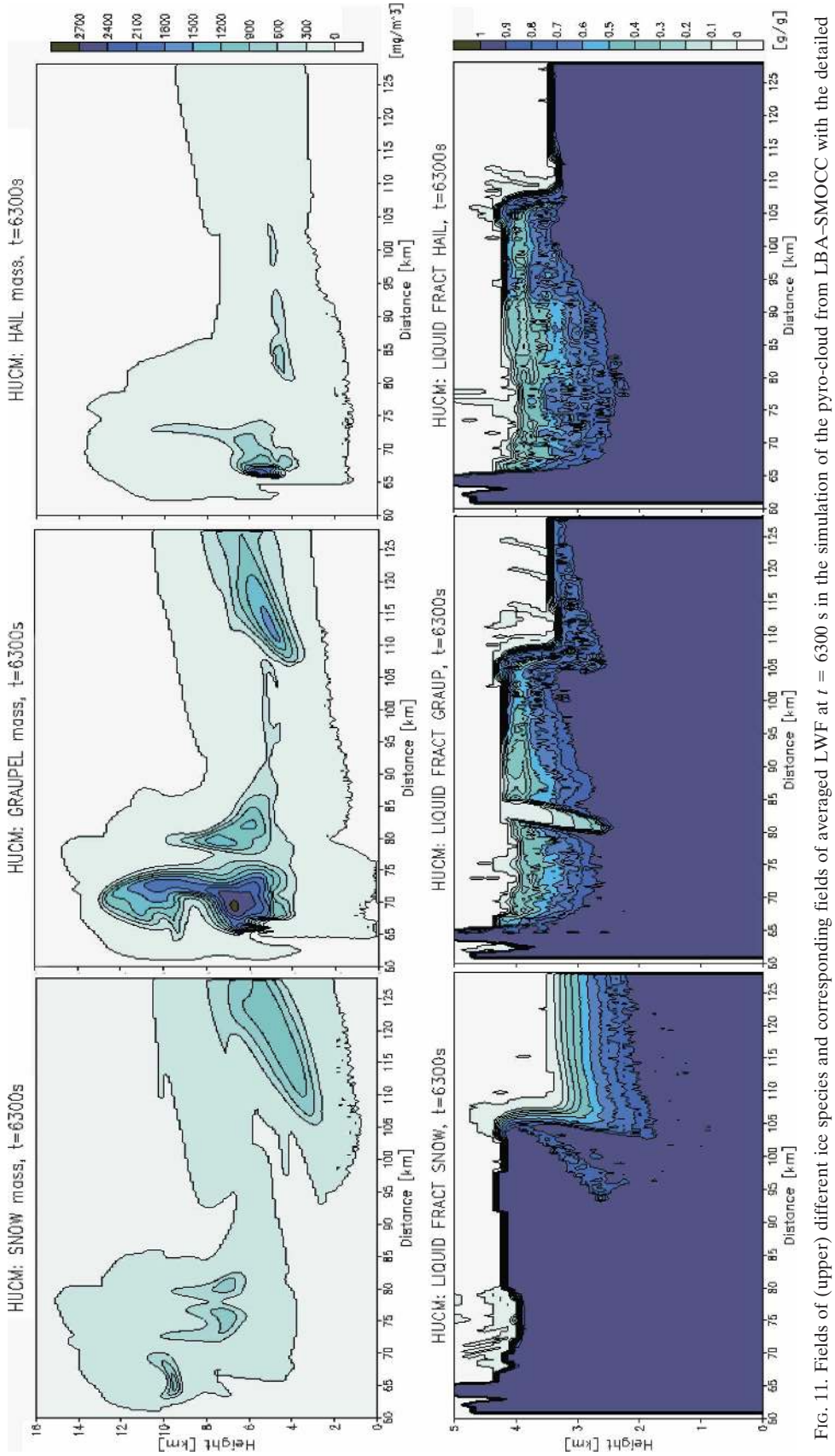

FIG. 11. Fields of (upper) different ice species and corresponding fields of averaged LWF at $t = 6300$ s in the simulation of the pyro-cloud from LBA–SMOCC with the detailed melting.

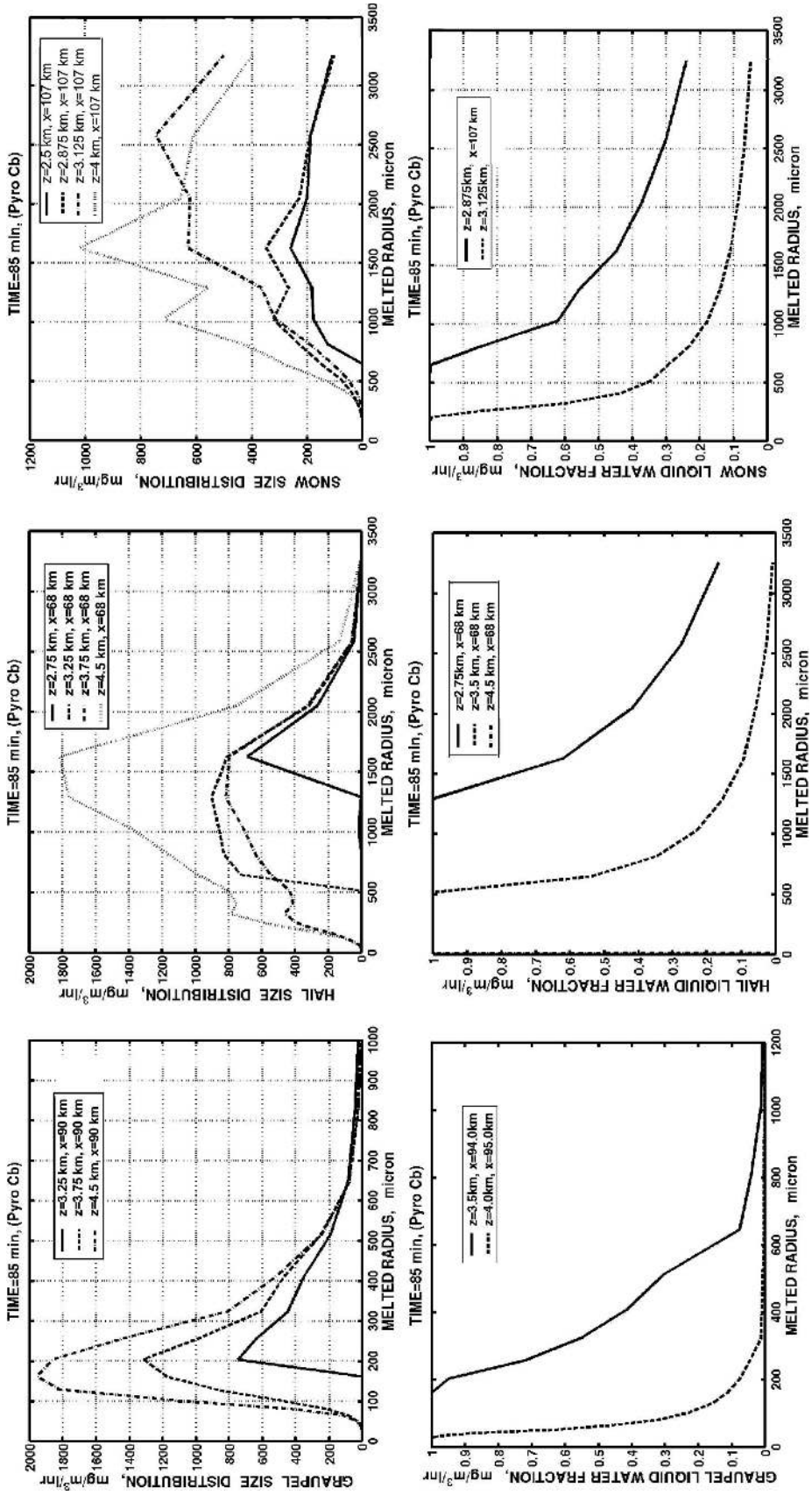

FIG. 12. (upper) Size distributions of graupel, hail/frozen drops, and snow, and size distributions of LWF in corresponding mass bins at different levels. LWF=0 corresponds to totally frozen particle, LWF = 1 correponds to totally melted particle. One can see that the process of melting starts with the smaller particles, so that at lower levels only the largest ones remain unmelted.

neous melting. There is more time for the ambient air to be cooled relative to cases of instantaneous melting. The low terminal velocity of ice must also contribute to the horizontal extent of the stratiform region (e.g., Liu et al. 1997) when it is melting, partially determining the horizontal distribution of melting-induced latent cooling. The detailed melting scheme accurately pre$_e$dicts the evolution of the terminal velocity of each particle during melting, which determines the temperature and humidity of the ambient air that ultimately drive all of its melting-related phase changes. This contrasts with the treatment of melting in most conventional schemes of bulk microphysics.

Second, the lower bulk density of melting ice particles means that they are larger, with a higher surface area for evaporation (a similar argument applies for sublimation before the delayed onset of melting), compared to raindrops of the same mass. Hence, the latent cooling rate from evaporation is higher relative to drops of the same mass [see Eqs. (2) and (18)]. (Of course, the fact that a raindrop's surface temperature at a given level below the freezing level is higher, than the surface temperature of the meltwater of a melting particle of the same mass, partially offsets some of this effect). Evaporation of meltwater during melting and sublimation before the onset of melting are expected to be very important for the overall impact on the heat budget from the choice of melting scheme, because the specific latent heats of evaporation and sublimation (2.5 and 2.8 MJ kg^{-1}) are an order of magnitude higher than that of melting (0.3 MJ kg^{-1}). Stronger latent cooling of the lower troposphere in regions where there are downdrafts, when detailed melting is included, tends to invigorate convection. The nature of this effect, however, depends on the thermodynamic conditions and environmental concentrations of aerosol.

However, it was found that the effect on cloud dynamics arising from melting is comparatively weak in maritime conditions and in green-ocean clouds. The common feature of such clouds is the rapid formation of precipitation at lower levels. Thus, warm rain represents the main fraction of precipitation. This general result is consistent with the findings from several previous studies showing that the fraction of melted to liquid precipitation is higher at higher environmental CCN concentrations (e.g., Khain and Pokrovsky 2004; see section 1). Moreover, precipitating particles fall in close vicinity to the cloudy updraft, so that enhancement of the vorticity field by dipoles of latent heating/cooling is quite weak. The generation of vorticity by dipoles of latent heating/cooling in the melting layer was found in simulations by Szyrmer and Zawadzki (1999).

The convective invigoration is found to be the greatest in clouds that developed in smoky (continental) air, since melting rates are higher when a greater mass of ice precipitation is generated at higher aerosol concentrations. Previous studies have shown that high CCN concentrations favor formation of rain at high subzero levels where it tends to freeze and of ice precipitation by cold-cloud processes (e.g., Reisin et al. 1996; see introduction). In the cases of Texas clouds and Amazonian smoky/pyro-clouds simulated here, the dominant contribution to precipitation is from melting of ice to form rain.

In particular, in the case of Texas clouds, formation of secondary cloud cells was found when detailed melting was included, with a corresponding increase in the amount of accumulated surface precipitation (an approximate doubling). Precipitation in this case remains, nevertheless, quite small, despite being doubled. In the context of a cloud ensemble, such effects on the precipitation must be transient if the net moistening from large-scale advection and surface evaporation are to be approximately balanced by surface precipitation in the mass budget of water substance on longer time scales than those simulated here. By contrast, in the pyro-cloud case, inclusion of detailed melting acted to decrease the amount of accumulated rain. This effect is explicable in terms of the invigoration of convection in the pyro-cloud that leads to a significant increase in the loss of ice mass by sublimation at upper levels. Extra sublimation of ice aloft then reduced the overall mass of ice reaching the freezing level. Both the wind shear and stability conditions of the environmental sounding applied in the simulation did not allow formation of secondary clouds in this case.

Finally, the variation of the fall speed during melting must be a major aspect of the vertical distribution of rates of latent cooling found in the cases of detailed melting, since the fall speed can be up to several times larger than the dry value for a liquid fraction of 50% (e.g., Mitra et al. 1990). Full advantage of a detailed description of the melting process, involving a calculation of the liquid fraction in ice particles across a range of sizes, will be achieved when it is extended to predict the radar scattering properties of melting particles. This will facilitate correct inference of precipitation rates and other aspects of stratiform cloud from meteorological radar observations.

Acknowledgments. This study was partially supported by the Israel Ministry of Science (the Germany–Israel collaboration in Water Resources, Grant W403) and the European Grant ANTISTORM. The first author was supported by the Atmospheric and Oceanic Sciences (AOS) Program of Princeton University.

REFERENCES

Andreae, M. O., D. Rosenfeld, P. Artaxo, A. A. Costa, G. P. Frank, K. M. Longlo, and M. A. F. Silva-Dias, 2004: Smoking rain clouds over the Amazon. *Science,* **303,** 1337–1342.

Atlas, D., R. Tatehira, R. C. Srivastava, W. Marker, and R. E. Carbone, 1969: Precipitation-induced mesoscale wind perturbations in the melting layer. *Quart. J. Roy. Meteor. Soc.,* **95,** 544–560.

Barth, M. C., and D. B. Parsons, 1996: Microphysical processes associated with intense frontal rainbands and the effect of evaporation and melting on frontal dynamics. *J. Atmos. Sci.,* **53,** 1569–1586.

Battan, L. J., 1973: *Radar Observation of the Atmosphere*. University of Chicago Press, 324 pp.

Bauer, P., A. Khain, A. Pokrovsky, R. Meneghini, C. Kummerow, F. Marzano, and J. P. V. Poiares Baptista, 2000: Combined cloud-microwave radiative transfer modeling of stratiform rainfall. *J. Atmos. Sci.,* **57,** 1082–1104.

Chen, J.-P., and D. Lamb, 1999: Simulation of cloud microphysical and chemical processes using a multicomponent framework. Part II: Microphysical evolution of a wintertime orographic cloud. *J. Atmos. Sci.,* **56,** 2293–2312.

Chen, S., and W. R. Cotton, 1988: The sensitivity of a simulated extratropical mesoscale convective system to longwave radiation and ice-phase microphysics. *J. Atmos. Sci.,* **45,** 3897–3910.

Fabry, F., and I. Zawadzki, 1995: The melting layer of precipitation: Radar observations and their interpretation. *J. Atmos. Sci.,* **52,** 838–851.

——, and W. Szyrmer, 1999: Modeling of the melting layer. Part II: Electromagnetic. *J. Atmos. Sci.,* **56,** 3593–3600.

Ferrier, B. S., and R. A. Houze, 1989: One-dimensional time dependent modeling of GATE cumulonimbus convection. *J. Atmos. Sci.,* **46,** 330–352.

Findeisen, W., 1940: The formation of the 0°C-isothermal layer and fractocumulus under nimbostratus. *Meteor. Z.,* **6,** 882–888.

Hudson, J. G., 1993: Cloud condensational nuclei near marine cumulus. *J. Geophys. Res.,* **98,** 2693–2702.

Khain, A. P., and I. Sednev, 1996: Simulation of precipitation formation in the Eastern Mediterranean coastal zone using a spectral microphysics cloud ensemble model. *Atmos. Res.,* **43,** 77–110.

——, and A. Pokrovsky, 2004: Effects of atmospheric aerosols on deep convective clouds as seen from simulations using a spectral microphysics mixed-phase cumulus cloud model. Part II: Sensitivity study. *J. Atmos. Sci.,* **61,** 2983–3001.

——, M. Ovtchinnikov, M. Pinsky, A. Pokrovsky, and H. Krugliak, 2000: Notes on the state-of-the-art numerical modeling of cloud microphysics. *Atmos. Res.,* **55,** 159–224.

——, D. Rosenfeld, and A. Pokrovsky, 2001: Simulation of deep convective clouds with sustained supercooled liquid water down to –37.5°C using a spectral microphysics model. *Geophys. Res. Lett.,* **28,** 3887–3890.

——, A. Pokrovsky, M. Pinsky, A. Seifert, and V. Phillips, 2004: Effects of atmospheric aerosols on deep convective clouds as seen from simulations using a spectral microphysics mixed-phase cumulus cloud model. Part I: Model description. *J. Atmos. Sci.,* **61,** 2963–2982.

Klaassen, W., 1988: Radar observations and simulation of the melting layer of precipitation. *J. Atmos. Sci.,* **45,** 3741–3753.

Knight, C. A., L. J. Miller, and W. D. Hall, 2004: Deep convection and "first echoes" within anvil precipitation. *Mon. Wea. Rev.,* **132,** 1877–1890.

Liu, C., M. W. Moncrieff, and E. J. Zipser, 1997: Dynamical influence of microphysics in tropical squall lines: A numerical study. *Mon. Wea. Rev.,* **125,** 2193–2210.

Martins, J. A., F. L. T. Gonzalves, J. C. P. Oliveira, A. A. Costa, J. B. V. Leal Junior, and M. A. Silva Dias, 2004: Cloud condensational nuclei in clear and polluted atmospheric conditions in the Amazonian region. *Proc. 14th Int. Conf. on Clouds and Precipitation,* Bologna, Italy, ICCP, 588–591.

Marwitz, J. D., 1983: The kinematics of orographic airflow during Sierra storms. *J. Atmos. Sci.,* **40,** 1218–1227.

Mitra, S. K., O. Vohl, M. Ahr, and H. R. Pruppacher, 1990: A wind tunnel and theoretical study of the melting behavior of atmospheric ice particles. Part IV: Experiment and theory for snow flakes. *J. Atmos. Sci.,* **47,** 584–591.

Moore, G. W., and R. E. Stewart, 1985: The coupling between melting and convective air motions in stratiform clouds. *J. Geophys. Res.,* **90,** 10 659–10 666.

Phillips, V. T. J., 2001: Simulations of the glaciation of a New Mexican storm cloud with an explicit microphysics model (EMM). Ph.D. thesis, University of Manchester School of Science and Technology, 199 pp.

——, A. M. Blyth, P. R. A. Brown, T. W. Choularton, and J. Latham, 2001: The glaciation of a cumulus cloud over New Mexico. *Quart. J. Roy. Meteor. Soc.,* **127,** 1513–1534.

——, T. W. Choularton, A. M. Blyth, and J. Latham, 2002: The influence of aerosol concentrations on the glaciation and precipitation of a cumulus cloud. *Quart. J. Roy. Meteor. Soc.,* **128,** 951–971.

——, ——, A. J. Illingworth, R. J. Hogan, and P. R. Field, 2003: Simulations of the glaciation of a frontal mixed-phase cloud with the Explicit Microphysics Model. *Quart. J. Roy. Meteor. Soc.,* **129,** 1351–1371.

——, and Coauthors, 2005: Anvil glaciation in a deep cumulus updraft over Florida simulated with an Explicit Microphysics Model. I: The impact of various nucleation processes. *Quart. J. Roy. Meteor. Soc.,* **131,** 2019–2046.

Pruppacher, H. R., and J. D. Klett, 1997: *Microphysics of Clouds and Precipitation*. 2d ed. Oxford University Press, 954 pp.

Rasmussen, R. M., and A. J. Heymsfield, 1987: Melting and shedding of graupel and hail. Part I: Model physics. *J. Atmos. Sci.,* **44,** 2754–2763.

——, V. Levizzani, and H. R. Pruppacher, 1984a: A wind tunnel and theoretical study of the melting behavior of atmospheric ice particles. Part II: A theoretical study for frozen drops of radius < 500 μm. *J. Atmos. Sci.,* **41,** 374–380.

——, ——, and ——, 1984b: A wind tunnel and theoretical study of the melting behavior of atmospheric ice particles. Part III: Experiment and theory for spherical ice particles of radius >500 μm. *J. Atmos. Sci.,* **41,** 381.

Rauber, R. M., L. S. Olthoff, M. K. Ramamurthy, and K. E. Kunkel, 2000: The relative importance of warm rain and melting processes in freezing precipitation events. *J. Appl. Meteor.,* **39,** 1185–1195.

Reisin, T., Z. Levin, and S. Tzivion, 1996: Rain production in convective clouds as simulated in an axisymmetric model with detailed microphysics. Part II: Effects of varying drops and ice initiation. *J. Atmos. Sci.,* **53,** 1815–1837.

Rissler, J., E. Swietlicki, J. Zhou, G. Roberts, M. O. Andreae, L. V. Gatti, and P. Artaxo, 2004: Physical properties of the sub-micrometer aerosol over the Amazon rain forest during the wet-to-dry season transition-comparison of modelled and

measured CCN concentrations. *Atmos. Chem. Phys. Discuss.,* **4,** 3159–3225.

Roberts, G. C., P. Artaxo, J. Zhou, E. Swetlicki, and M. O. Andreae, 2002: Sensitivity of CCN spectra on chemical and physical properties of aerosol: A case study from the Amazon Basin. *J. Geophys. Res.,* **107,** 8070, doi:10.1029/2001JD000583.

Rosenfeld, D., and W. Woodley, 2000: Deep convective clouds with sustained supercooled liquid water down to –37.5°C. *Nature,* **405,** 440–442.

Stewart, R. E., and S. R. Macpherson, 1989: Winter storm structure and melting-induced circulations. *Atmos.–Ocean,* **27** (1), 5–23.

——, J. D. Marwitz, J. E. Pace, and R. E. Carbone, 1984: Characteristics through the melting layer of stratiform clouds. *J. Atmos. Sci.,* **41,** 3227–3237.

——, R. Crawford, K. K. Szeto, and D. Hudak, 1996: Horizontal aircraft passes across 0°C regions within winter storms. *Atmos.–Ocean,* **34,** 133–159.

Szeto, K. K., and R. E. Stewart, 1997: Effects of melting on frontogenesis. *J. Atmos. Sci.,* **54,** 689–702.

——, ——, and C. A. Lin, 1988: Mesoscale circulations forced by the melting of snow in the atmosphere. Part II: Application to meteorological features. *J. Atmos. Sci.,* **45,** 1642–1650.

Szyrmer, W., and I. Zawadzki, 1999: Modeling of the melting layer. Part I: Dynamics and microphysics. *J. Atmos. Sci.,* **56,** 3573–3592.

Tao, W.-K., J. Simpson, and S.-T. Soong, 1991: Numerical simulation of a subtropical squall line over the Taiwan Strait. *Mon. Wea. Rev.,* **119,** 2699–2723.

Turpeinen, O., and M. K. Yau, 1981: Comparison of results from a three-dimensional cloud model with statistics of radar echoes on day 261 of GATE. *Mon. Wea. Rev.,* **109,** 1495–1511.

Wang, P. K., and W. Ji, 1992: A numerical study of the diffusional growth and riming rates of ice crystals in clouds. *Proc. 11th Int. Conf. on Clouds and Precipitation,* Montreal, QC, Canada, ICCP, 76–77.

Wexler, R., R. J. Reed, and J. Honig, 1954: Atmospheric cooling by melting snow. *Bull. Amer. Meteor. Soc.,* **35,** 48–51.

Willis, P. T., and A. J. Heymsfield, 1989: Structure of the melting layer in mesoscale convective system stratiform precipitation. *J. Atmos. Sci.,* **46,** 2008–2025.

Ziegler, C. L., 1988: Retrieval of thermal and microphysical variables in observed convective storms. Part II: Sensitivity of cloud processes to variation of the microphysical parameterization. *J. Atmos. Sci.,* **45,** 1072–1090.